How well can hillslope models 'explain' topography? Simulating soil transport and production with high-resolution topographic data

Article *in* Geological Society of America Bulletin · September 2008

DOI: 10.1130/B26283.1

CITATIONS
183

READS
1,154

1 author:

Josh Roering
University of Oregon
192 PUBLICATIONS **9,137** CITATIONS

SEE PROFILE

How well can hillslope evolution models "explain" topography? Simulating soil transport and production with high-resolution topographic data

Joshua J. Roering
Department of Geological Sciences, University of Oregon, Eugene, Oregon 97403-1272, USA

ABSTRACT

The morphology of hillslopes is a direct reflection of tectonic forcing and climatic and biologic processes that drive soil production, mobilization, and transport. Soil transport on hillslopes affects river incision by providing tools for channel abrasion and controls the distribution of sediment that influences aquatic habitat. Although numerous hillslope transport relationships have been proposed over the past 60+ years, a comprehensive analysis of model predictions for a real landscape has not been performed. Here, we use high-resolution topographic data obtained via airborne laser swath mapping (ALSM) to simulate the long-term evolution of Oregon Coast Range hillslopes and test three published transport models and a new model that accounts for nonlinear depth- and slope-dependent transport. Analysis of one-dimensional, steady-state solutions for these four models suggests that plots of gradient-curvature may be diagnostic for distinguishing model predictions. To evaluate two-dimensional model predictions for our field site, we assumed local steady-state erosion for a 72,000 m^2 sequence of hillslopes and valleys. After calibrating each of the four models, we imposed constant base-level lowering for cells within the valley network, simulated 500,000 yr of soil production and transport, and determined which transport model best preserved morphologic patterns that describe the current landscape form. Models for which flux varies proportionally with hillslope gradient generated broadly convex hilltops inconsistent with the sharp-crested, steep-sided slopes of our study site, whereas the two nonlinear slope-dependent models produced convex-planar slopes consistent with current hillslope form. Our proposed nonlinear slope- and depth-dependent model accounts for how soil thickness controls the magnitude of biogenic disturbances that drive transport; this model best preserved the current landscape form, particularly the narrow, sharply convex hilltops characteristic of the Oregon Coast Range. According to our formulation, which provides an explicit linkage for relating the distribution of biota to hillslope processes, the degree of hilltop convexity varies nonlinearly with the ratio of erosion rate to maximum soil production rate, highlighting the profound influence of soil depth on hillslope evolution.

Keywords: hillslope evolution, soil transport, nonlinear transport, airborne lidar.

INTRODUCTION

In hilly and mountainous landscapes, the downslope movement of soil on hillslopes modulates landscape form and sediment delivery to channels. The coupling between rock uplift and topographic relief thus depends on the efficacy of diverse climate-related hillslope processes, such as frost heave, bioturbation, and shallow landsliding. With increasing rates of rock uplift and erosion, for example, mass wasting processes promote rapid sediment fluxes on steep slopes and may limit further topographic development (e.g., Burbank et al., 1996; Montgomery and Brandon, 2002). As a result, deciphering rates of tectonic forcing from topographic metrics requires information on hillslope process mechanics and rates (e.g., Ahnert, 1970b; Ahnert, 1984; Whipple et al., 2005). In the absence of overland flow, mass transport on soil-mantled slopes is often driven by disturbances associated with biological activity (i.e., bioturbation). This explicit linkage between biology and sediment transport suggests that ecological changes associated with long-term climatic fluctuations may induce first-order shifts in hillslope form and sediment yield (Gabet et al., 2003; Roering et al., 2004; Yoo et al., 2005). Quantitatively exploring these feedbacks between hillslope topography and climatic and tectonic processes requires that we posit equations to represent transport on hillslopes, an endeavor that has occupied geologists for nearly 100 yr.

In 1909, G.K. Gilbert (Gilbert, 1909) expounded upon the ideas of Davis (1892) and proposed a process-based explanation for the convex form of "debris"-mantled hillslopes. For a one-dimensional hillslope that erodes at a spatially constant rate, sediment flux must increase linearly with distance from the drainage divide (i.e., hilltop). To accommodate the progressive downslope increase in flux, slopes become monotonically steeper as increasing gravitational acceleration facilitates transport via disturbances (such as those associated with biogenic activity). The progressive downslope increase in slope angle defines a convex form between hilltops and channels, which is commonly observed for natural slopes. Several decades after Gilbert's work, his conceptual framework was cast into equations by Culling (1963) and since the 1960s, dozens of quantitative hillslope evolution models have emerged, virtually all of which incorporate slope angle as the primary control on sediment transport rates (e.g., Ahnert, 1976; Arrowsmith et al., 1996; Avouac and Peltzer, 1993; Braun and Sambridge, 1997; Culling, 1963; Dietrich and Perron, 2006; Hanks, 2000; Howard, 1997; Istanbulluoglu et al., 2004; Kirkby, 1971; Kooi and Beaumont, 1994; Koons, 1989; Tucker and Slingerland, 1994; van der Beek and Braun, 1998; Willett, 1999; Willgoose et al., 1991).

Linear slope-dependent transport models predict convex hillslopes and have a straightforward mathematical form, making them simple to implement in analytical and numerical models of landscape evolution (Koons, 1989). Importantly, linear models predict that steady-state hillslopes exhibit constant curvature (Fernandes and Dietrich, 1997). Despite the

†E-mail: jroering@uoregon.edu

GSA Bulletin; September/October 2008; v. 120; no. 9/10; p. 1248–1262; doi: 10.1130/B26283.1; 12 figures; 1 table.

visually and computationally appealing nature of the linear transport model, the prediction of constant curvature slopes is inconsistent with frequently observed convex-planar slopes in soil-mantled regions (Carson and Petley, 1970; Penck, 1953; Strahler, 1950; Young, 1961). To account for this discrepancy, a raft of transport models emerged in the 1980s and 1990s; these models incorporated a nonlinearity in the flux-slope relationship such that transport rates increase rapidly as slopes approach a critical angle (Anderson, 1994; Anderson and Humphrey, 1989; Andrews and Bucknam, 1987; Gabet, 2000; Howard, 1994; Kirkby, 1984; Roering et al., 1999). Put simply, the flux-slope nonlinearity enables nearly steep and planar (low convexity) sideslopes to erode at rates commensurate with highly convex hilltops. More recently, several studies have proposed that flux rates depend on slope angle and soil depth (e.g., Furbish and Fagherazzi, 2001; Heimsath et al., 2002; Heimsath et al., 2005; Mudd and Furbish, 2007; Yoo et al., 2005), enabling these models to be directly coupled with representations of depth-dependent biological processes.

Despite the widespread availability of computational resources and high-resolution topographic data (via airborne laser altimetry), few studies have simulated the evolution of "real" landscapes at the process scale to test hillslope transport models (Ahnert, 1970a; Braun et al., 2001; Dietrich et al., 2003; Herman and Braun, 2006; Minasny and McBratney, 2006). In most geological settings, this endeavor is challenging because we lack quantitative information on the original hillslope form necessary for model initialization. Dietrich et al. (2003) used airborne light detection and ranging (LiDAR)-generated topography of Oregon Coast Range slopes as the initial condition and applied a nonlinear, slope-dependent transport model and exponential soil production model to simulate one million years of hillslope evolution driven by base-level lowering of the valley network. Using the assumption of locally steady-state topography, they compared their results with the initial topographic form (i.e., current topography) to assess model success. Essentially, they inquired as to how well a previously calibrated transport model can preserve current landscape form. Here, we adopt a similar approach, but instead test a diverse suite of representative transport models to systematically determine which best preserves diagnostic properties of current topography in the Oregon Coast Range. We also propose a new transport model for which flux depends nonlinearly on slope and soil depth. Because the depth dependency depends on the vertical distribution of biological activity in soil, this new formulation enables us to calibrate and test the model with field-generated biological data. Our results are useful for predicting sediment yield to channel networks as well as interpreting and predicting morphologic response to tectonic and climatic perturbations in real landscapes.

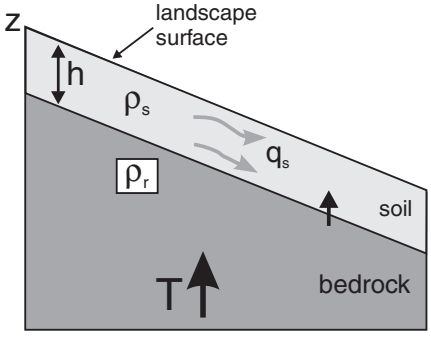

Figure 1. Schematic diagram of mass conservation components in a soil-mantled landscape. See Equations 1 and 2 for explanation.

MASS CONSERVATION LAWS FOR HILLSLOPE EVOLUTION

Landscapes result from the coupled influence of tectonic forcing, which displaces bedrock both vertically and horizontally, and geomorphic processes that both convert substrate into mobile material and transport that material across the surface (Dietrich et al., 2003). According to a mass conservation Equation that accounts for these processes, the rate of change of the surface elevation, z, is given by:

$$\frac{\partial z}{\partial t} = T - \frac{\rho_r}{\rho_s}\varepsilon + \frac{\partial h}{\partial t}, \quad (1)$$

where t is time, T is rock uplift rate (L T^{-1}), ε is sediment (or soil) production rate (L T^{-1}), h is vertical soil depth (L), and ρ_r and ρ_s are the bulk densities of rock and soil, (M L^{-3}), respectively (Fig. 1). On hillslopes, the change in the soil thickness with time depends on the balance of erosion by soil transport, $\tilde{q}_s$, (L^3 L^{-1} T^{-1}) and the soil production rate:

$$\frac{\partial h}{\partial t} = -\nabla \cdot \tilde{q}_s + \frac{\rho_r}{\rho_s}\varepsilon. \quad (2)$$

These equations do not account for mass loss via chemical weathering, which will affect the bulk densities of soil and bedrock as well as the "erodibility" of bedrock as represented by ε. If erosion (denoted here as $-\nabla \cdot \tilde{q}_s$) outpaces soil production, bedrock emerges and erosion is limited by the maximum soil production rate.

SOIL PRODUCTION MODEL

The presence or absence of soil has a profound influence on the mechanics and rates of surficial processes as well as feedbacks with ecological processes. Following insights first proposed by Gilbert (1877), recent studies have demonstrated that the rate of soil production, ε, declines exponentially with slope-normal soil depth according to:

$$\varepsilon = \frac{\varepsilon_0}{\cos\theta} e^{-\mu h \cos\theta}, \quad (3)$$

where ε_0 is the maximum production rate associated with zero soil depth, μ is the exponential decay constant, and θ is local slope in degrees (Heimsath et al., 2001b). The cosine term in the exponential function is included to convert vertical soil depth to slope-normal soil depth and the cosine term in the denominator is included to convert soil production measured slope-normal into a vertical reference frame. Here, we express soil depth, h, in a vertical orientation to facilitate presentation and interpretation of our simulation results. Equation 3 is equivalent to Equation 5 in Heimsath et al. (2001b).

On a steady-state hillslope (i.e., $\partial h/\partial t = 0$) for which the erosion rate ($E = -\nabla \cdot \tilde{q}_s$) is spatially uniform, such that $E = \varepsilon$, steady-state soil depth is given by:

$$h = \frac{-\ln\left(\frac{E}{\varepsilon_0}\cos\theta\right)}{\mu\cos\theta}. \quad (4)$$

Equation 4 indicates that steady-state soil depth is not constant, but in fact varies systematically with slope angle. To explore the magnitude of this effect, we can rewrite Equation 4 in terms of dimensionless soil depth, h^*:

$$h^* = h\mu = \frac{-\ln\left(\frac{E}{\varepsilon_0}\cos\theta\right)}{\cos\theta}. \quad (5)$$

The value of h^* decreases nonlinearly with E/ε_0 such that the change in h^* along a single hillslope is greatest when E/ε_0 is small and the slope is steep (Fig. 2). Due to the onset of shallow landsliding, the soil mantle may become patchy and tenuous for slope gradients greater than 1.0. Thus, the range of applicability for this relationship varies with factors that control shallow landslide susceptibility, including soil properties, root reinforcement via vegetation, and rainfall characteristics. Interestingly,

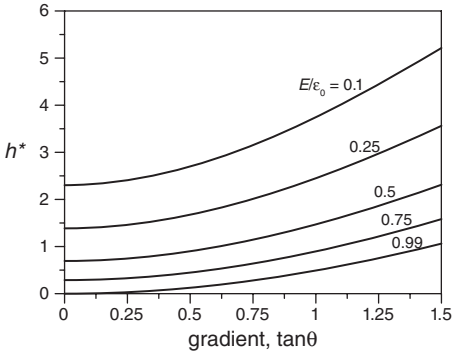

Figure 2. Variation of dimensionless soil depth (h^*) with hillslope gradient as given in Equation 5. Soil depth is defined as vertical. Soil depth increases nonlinearly downslope and for a given slope angle, soil depth decreases as the ratio of steady-state erosion rate to maximum soil production rate (E/ε_0) increases.

as $E/\varepsilon_0 \rightarrow 1$, h^* values approach zero near the hilltop (i.e., where $\theta = 0$). Accordingly, if the rate of baselevel lowering increases and $E/\varepsilon_0 \geq 1$, Equation 5 predicts that the soil mantle will initially be stripped from hilltops rather than sideslopes that are more directly coupled to channels.

SOIL TRANSPORT MODELS

On hillslopes, the transport of soil in the absence of overland flow has been described by a diverse suite of equations (e.g., Dietrich and Perron, 2006). Numerous models have been proposed, but here we focus on four representative transport models that encapsulate a range of mechanical behavior. We do not include slopewash models in this analysis because overland flow erosion is not relevant to our field site in the Oregon Coast Range.

Linear Slope-Dependent Model

The linear, slope-dependent model was first proposed by Culling (1960) and has been used extensively in landscape evolution models. According to this model, sediment flux varies proportionally with local gradient, ∇z, where K_1 is a constant of proportionality with units $L^2\ T^{-1}$:

$$\tilde{q}_s = -K_1 \nabla z \ . \qquad (6)$$

As demonstrated below, Equation 6 predicts that hillslopes attain constant curvature given steady-state erosion.

Depth-Slope Product Model

Because transporting agents are relegated to the thickness of available soil (measured normal to slope as $h\cos\theta$), studies that account for particle activation via disturbances and particle density variations with depth propose that flux can be represented with the depth-slope product (Ahnert, 1976; Braun et al., 2001; Furbish and Fagherazzi, 2001; Heimsath et al., 2005; Mudd and Furbish, 2007) according to:

$$\tilde{q}_s = -K_2 h \cos\theta \nabla z, \qquad (7)$$

where K_2 is a transport rate coefficient with units $L\ T^{-1}$ and h is specified as the active soil depth (L). The active soil depth can presumably be estimated from field-based documentation of relevant transport processes.

Nonlinear Slope-Dependent Model

Given the ubiquity of convex-planar slopes, numerous models have proposed that transport varies nonlinearly with gradient such that fluxes increase rapidly as slope angle approaches a critical value (Anderson, 1994; Howard, 1994). Initially, this nonlinearity was proposed to account for the increasing frequency of landslides as slopes approach the angle of repose. Experimental evidence indicates, however, that landsliding is not required to generate the nonlinearity (Roering et al., 2001b), which instead may result from the interplay between friction and gravity in a surface layer undergoing disturbance. A physically based model proposed by Andrews and Bucknam (1987) and recast by Roering et al. (1999) indicates that flux varies according to:

$$\tilde{q}_s = \frac{-K_3 \nabla z}{1 - \left(|\nabla z| / S_c\right)^2}, \qquad (8)$$

where S_c is the critical gradient at which flux becomes infinite and K_3 is a transport coefficient ($L^2\ T^{-1}$) given by:

$$K_3 = \frac{2}{\rho_s g S_c^2} P_A, \qquad (9)$$

where P_A is power per unit area ($ML^2\ T^{-3}\ L^{-2}$) generated by disturbances that drive soil transport and g is acceleration due to gravity ($L\ T^{-2}$). Equation 9 provides a framework for quantitatively linking the magnitude of transport with processes that mobilize and transport soil in real landscapes.

Nonlinear Depth- and Slope-Dependent Model

Here, we propose a revision to the nonlinear slope-dependent model by relating P_A to the vertical distribution of transport-inducing agents in a column of soil. Analogous to the formulation of Yoo et al. (2005), we can partition P_A into the product of power per unit volume of disturbance agents, P_V ($ML^2\ T^{-3}\ L^{-3}$), and the total volume of disturbance agents per unit area, D_A (L^3/L^2):

$$P_A = D_A P_V . \qquad (10)$$

Equation 10 indicates that for a column of soil, we can depth integrate the volume of disturbance agents to estimate P_A. Given that biological organisms, frost heave activity, and other transport agents tend to vary systematically with depth, we can calculate D_A by integrating the distribution of these agents (through the depth of available soil measured normal to the surface, $h\cos\theta$) according to:

$$D_A = \int_0^{h\cos\theta} D_z dz', \qquad (11)$$

where D_z is the volume of disturbance agents per unit volume of soil (L^3/L^3) and z' is the axis oriented normal to the surface. Equations 10 and 11 enable us to link our transport model with field-based estimates of how disturbance agents are distributed with depth. In vegetated landscapes, for example, root growth causes soil particle activation, mobilization, and downslope transport (Gabet et al., 2003), suggesting that profiles of root density may be useful for estimating soil transport rates. Commonly, root density declines exponentially with depth measured normal to the surface (e.g., Canadell et al., 1996; Jackson et al., 1996) such that D_z can be defined according to

$$D_z = \alpha e^{-\beta z'}, \qquad (12)$$

where α is the density of roots at the surface ($L^3\ L^{-3}$) and β, which has units L^{-1}, describes the rate of exponential decline with depth. Combining Equations 11 and 12 and integrating through the normal soil thickness yields an expression for D_A:

$$D_A = \int_0^{h\cos\theta} \alpha e^{-\beta z'} dz' = \frac{\alpha}{\beta}\left(1 - e^{-\beta h \cos\theta}\right). \qquad (13)$$

Equation 13 can be combined with Equations 9 and 10, producing an expression for a new transport coefficient, K_4, which varies according to:

$$K_4(h) = \frac{2\alpha P_V}{\beta g S_c^2 \rho_s}\left(1 - e^{-\beta h \cos\theta}\right) = \eta\left(1 - e^{-\beta h \cos\theta}\right). \quad (14)$$

Rewriting Equation 8 in terms of K_4 yields:

$$\tilde{q}_s = \frac{-K_4(h)\nabla z}{1 - \left(|\nabla z|/S_c\right)^2}. \quad (15)$$

To illustrate how K_4 depends on soil thickness, we normalized Equation 14 as follows:

$$K_4^* = \frac{K_4}{\eta} = \left(1 - e^{-\beta h \cos\theta}\right). \quad (16)$$

Equation 16 indicates that K_4^* increases rapidly with soil depth measured normal to the surface and approaches a constant value such that subsequent increases in soil depth result in negligible increases in flux (Fig. 3). Importantly, Equation 12 can take on any functional form that reflects the vertical distribution of relevant transport agents in a particular field setting. Here, we chose an exponential function because of its ubiquitous use in describing the distribution of biological agents in soil (Canadell et al., 1996; Gabet et al., 2003; Jackson et al., 1996). In the presence of multiple transport agents, Equation 10 can be used to calculate P_A as the sum of power per unit area for individual agents, i.e., $P_{A(\text{Total})} = (D_A P_V)_1 + (D_A P_V)_2 + \ldots + (D_A P_V)_N$.

MODEL IMPLICATIONS FOR ONE-DIMENSIONAL, STEADY-STATE MORPHOLOGY

The transport models expressed by Equations 6, 7, 8, and 15 have profound implications for the evolution of real landscapes. Before embarking on a series of two-dimensional simulations, however, it is instructive to explore the morphologic predictions of these models using a one-dimensional, steady-state approximation. For this comparison, we use the steady-state relationship between gradient and curvature for each of the models to distinguish their behavior because: (1) analytical expressions for one-dimensional, gradient-curvature relationships can be readily derived, (2) gradient and curvature are easily estimated from topographic data for real landscapes, and (3) gradient-curvature curves appear to be diagnostic for distinguishing model predictions. Although this one-dimensional approach cannot account for variations in planform curvature that are characteristic of many natural hillslopes, it does provide a first-order framework for exploring model predictions. For a one-dimensional, steady-state hillslope (such that the rates of rock uplift and erosion are equivalent, i.e., $\partial z/\partial t = 0$ and $T = -E$), Equations 1 and 2 can be combined and simplified as:

$$\frac{dq_s}{dx} = \frac{\rho_r}{\rho_s} E. \quad (17)$$

By individually substituting one-dimensional versions of Equations 6, 7, 8, and 15 into Equation 17, we obtain a series of expressions for steady-state hillslope curvature as a function of gradient and erosion rate. Because two of the flux models (Equations 7 and 15) depend on soil depth, the steady-state soil depth (Equation 4) is substituted into those equations prior to differentiation. One-dimensional curvature for the K_1, K_2, K_3, and K_4 (or η) models, respectively, varies according to:

$$\frac{d^2z}{dx^2} = -\frac{\rho_r}{\rho_s}\frac{E}{K_1} \quad (18a)$$

$$\frac{d^2z}{dx^2} = \frac{-\mu\frac{\rho_r}{\rho_s}\frac{E}{K_2}}{\left(\frac{(dz/dx)^2}{D_1}\right) - \ln\left(\frac{E}{\varepsilon_0\sqrt{D_1}}\right)} \quad (18b)$$

where $D_1 = 1 + (dz/dx)^2$,

$$\frac{d^2z}{dx^2} = \frac{-\frac{\rho_r}{\rho_s}\frac{E}{K_3}\left(1 - \left(\frac{dz/dx}{S_c}\right)^2\right)^2}{1 + \left(\frac{dz/dx}{S_c}\right)^2} \quad (18c)$$

$$\frac{d^2z}{dx^2} = \frac{-\frac{\rho_r}{\rho_s}\frac{E}{\eta}}{\left(\frac{\left[D_1^2(1-D_2)\right] + \left[\frac{\beta}{\mu}D_2\left(\frac{dz}{dx}\right)^2\left(1 - \left(\frac{dz/dx}{S_c}\right)^2\right)\right]}{D_1\left(1 - \left(\frac{dz/dx}{S_c}\right)^2\right)^2}\right)} \quad (18d)$$

where $D_2 = e^{(\beta/\mu)\ln\left((E/\varepsilon_0)/\sqrt{D_1}\right)}$.

To directly compare these predictions, we respectively normalized values of curvature calculated in Equations 18a–18d by the hilltop curvature $(d^2z/dx^2)_{HT}$, defined as d^2z/dx^2 evaluated at $dz/dx = 0$. For each of the four transport models, dimensionless curvature, C^*, is calculated from the general form, $C^* = -(d^2z/dx^2)/(d^2z/dx^2)_{HT}$:

$$C_1^* = -1 \quad (19a)$$

$$C_2^* = \frac{\ln\left(E/\varepsilon_0\right)}{\left[\left(\frac{(dz/dx)^2}{D_1}\right) - \ln\left(\frac{E}{\varepsilon_0\sqrt{D_1}}\right)\right]} \quad (19b)$$

$$C_3^* = \frac{-\left(1 - \left(\frac{dz/dx}{S_c}\right)^2\right)^2}{1 + \left(\frac{dz/dx}{S_c}\right)^2} \quad (19c)$$

$$C_4^* = \frac{-\left(1 - e^{(\beta/\mu)\ln(E/\varepsilon_0)}\right)D_1\left(1 - \left(\frac{dz/dx}{S_c}\right)^2\right)^2}{\left[D_1^2(1-D_2)\right] + \left[\frac{\beta}{\mu}D_2\left(\frac{dz}{dx}\right)^2\left(1 - \left(\frac{dz/dx}{S_c}\right)^2\right)\right]}. \quad (19d)$$

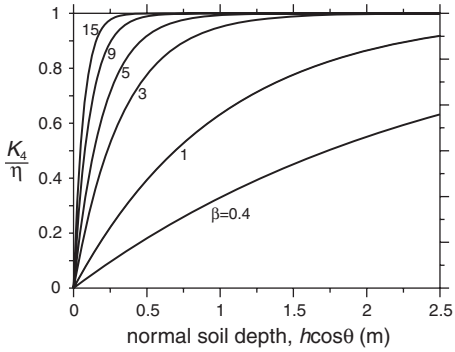

Figure 3. Variation of the dimensionless coefficient of the nonlinear slope- and depth-dependent (K_4) model with soil depth as given in Equation 16. For large values of β, transport rates increase rapidly with depth.

The negative value is included such that values of C^* are consistent with negatively curved (i.e., nonconcave) hillslopes. Equations 19a–19d provide a straightforward framework for comparing morphological implications of the four transport models assuming steady-state conditions (Fig. 4). As shown previously (Fernandes and Dietrich, 1997; Roering et al., 1999), convexity (negative curvature values) is invariant according to the linear, slope-dependent model (Equation 6), and C_1^* values are everywhere equal to −1 (Fig. 4A). In contrast, the depth-slope product model predicts that C_2^* values approach zero with increasing gradient. For

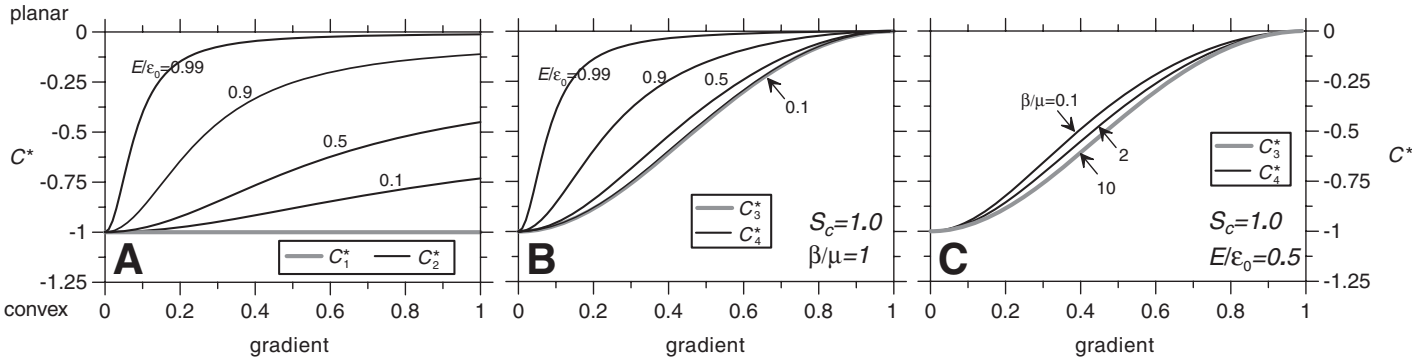

Figure 4. Variation of dimensionless curvature (C^*) with hillslope gradient for one-dimensional, steady-state hillslopes with uniform erosion. (A) The K_1 model predicts that C_1^* is constant, and the K_2 model predicts that C_2* approaches zero with slope depending on the value of E/ε_0. (B) and (C) The K_3 model predicts an invariant, sigmoidal curve where $S_c = 1.0$, whereas the K_4 model predicts that C_4^* values approach zero in a different fashion depending on the values of β and E/ε_0.

high ratios of erosion rate to maximum soil production rate ($E/\varepsilon_0 > 0.9$), the transition between high-convexity slopes and relatively planar ones is abrupt and occurs at low gradients. Morphologically, this gradient-curvature relationship corresponds to a hillslope with a sharply curved divide and effectively planar sideslopes. This pattern results from near-zero soil depths at the hilltop (Fig. 2), causing the depth component of transport to be negligible (see Equation 7) such that erosion must be accommodated by high convexity (i.e., rapid change in gradient at the hilltop). Moving off the divide to locations where gradients exceed 0.3, the downslope increase in flux necessary to maintain a steady-state condition can be accommodated by the incremental increase in soil depth (see Fig. 2) combined with small changes in gradient. With decreasing E/ε_0, the downslope decline in convexity with steepness is more gradual and for $E/\varepsilon_0 = 0.1$, hillslopes with gradient equal to 1.0 are only slightly less convex than hilltops.

The nonlinear, slope-dependent model (Equation 8) predicts a sigmoidal relationship between gradient and curvature and a gradual transition between convex hilltops and steep, planar sideslopes (see C_3^* curve in Fig. 4B). Owing to the condition of infinite flux when $|dz/dx| = S_c$, this model predicts that slopes become effectively planar as angles approach S_c. Once S_c is specified (here we use $S_c = 1.0$ for simplicity), Equation 19c indicates that the form of the gradient-curvature curve is fixed. In contrast, the nonlinear slope- and depth-dependent model (Equation 15) indicates that the gradient-curvature relationship (Equation 19d) depends on the value of S_c as well as β/μ and E/ε_0. Figure 4B shows that C_4^* values approach zero gradually for $E/\varepsilon_0 < 0.9$, whereas when $E/\varepsilon_0 > 0.9$, the convex-planar transition is rapid and occurs at low gradients, similar to predictions of the depth-slope product model (C_2^* curve in Fig. 4A). When $E/\varepsilon_0 < 0.9$, increasing values of β/μ cause the C_4^* curve to approach the C_3^* curve (Fig. 4C). This correspondence is intuitively appealing given that for high values of β relative to μ, fluxes depend weakly on soil depth. Finally, our analyses (Figs. 4B and 4C) indicate that C_4^* approaches C_3^* when $E/\varepsilon_0 < 0.5$ and $\beta/\mu > 2$.

These results suggest that the transport models outlined above predict diagnostic gradient-curvature relationships that should be useful for assessing model applicability to real landscapes. Interestingly, as erosion rates approach the maximum soil production rate ($E/\varepsilon_0 > 0.9$), the two flux equations that incorporate soil depth (Equations 7 and 15) predict similar steady-state, gradient-curvature relationships reflecting the profound influence of soil depth-dependent processes on hillslope form and evolution (see C_2^* and C_4^* curves in Figs. 4A and 4B). Below, we apply the two-dimensional versions of these models to the Oregon Coast Range to further explore the implications of different flux equations on slope morphology.

STUDY AREA

The Oregon Coast Range is a humid, soil-mantled, mountainous landscape largely composed of Eocene sedimentary rocks that overlie volcanic basement accreted to the North American plate in the early Tertiary (Orr et al., 1992). The area is almost exclusively underlain by the Tyee Formation, which has been studied in detail because of its distinct assemblage of sedimentary facies (Chan and Dott, 1983; Heller and Dickinson, 1985; Lovell, 1969). Heller and Dickinson (1985) suggested that the Tyee Formation is a sand-rich sequence of turbidite deposits originated from a delta-fed submarine ramp depositional system. Since the late Eocene, the Tyee Formation has been compressed into a series of low-amplitude, gently dipping folds (the maximum dip of bedding along the flanks of folds rarely exceeds 15°–20°) oriented north-northeast (Baldwin, 1956). Uplift of the Oregon Coast Range commenced in the Miocene (McNeill et al., 2000) and continues today as evidenced by abandoned wave-cut platforms along the Oregon coast (Kelsey et al., 1996). Rates of rock uplift derived via dating of marine terraces adjacent to our study area (latitude ranging from 43° to 45°) vary from <0.1 to 0.3 mm yr^{-1} (Kelsey et al., 1996) and are generally an order of magnitude lower than geodetic uplift rates derived from highway leveling and tide gauge data (Mitchell et al., 1994). Both short- and long-term uplift rates measured along the coast vary locally due to vertical movement along faults, although it is unclear whether these local variations extend a significant distance inland.

The topography of the Oregon Coast Range has been characterized as steep and highly dissected with broad regions of relatively uniform ridge and valley terrain (Dietrich and Dunne, 1978; Montgomery, 2001; Reneau and Dietrich, 1991). Typically, soil is relatively thin (~0.4 m) on hilltops and sideslopes and thicker (~1–2 m) in unchanneled valleys that act as preferential source areas for shallow landslides that often initiate debris flows (Dietrich and Dunne, 1978; Heimsath et al., 2001a). Soil transport and production appear to be driven primarily by biogenic processes, and overland flow on slopes is absent owing to highly permeable soils. Most studies of decadal- to millennial-scale patterns of sediment production and delivery in the Oregon Coast Range have focused on the cyclic infilling and evacuation of soil in steep, convergent areas (Benda and Dunne, 1997; Dietrich and Dunne, 1978; Reneau and Dietrich, 1990). Erosion rates generated by short (~10 yr) and

long-term (~5000 yr) analyses of sediment yield are commonly 0.05–0.25 mm yr−1 (Beschta, 1978; Bierman et al., 2001; Heimsath et al., 2001b; Reneau and Dietrich, 1991), consistent with rates of coastal uplift (Kelsey et al., 1996) and Holocene bedrock channel incision (Personius, 1995). These studies have been used to argue that an approximate balance exists between rock uplift and erosion in the Oregon Coast Range such that the topographic form may be relatively uniform with time (Montgomery, 2001; Reneau and Dietrich, 1991). This approximate balance is best reflected in the ubiquity of consistently spaced ridge and valley terrain in local areas. In contrast, deep-seated landslides (Roering et al., 2005), fluvial terrace remnants, and debris flow fans produce topographic features that persist for 10–100 k.y., and temporal patterns of sediment production associated with these transient features are unconstrained.

METHODS

To test how well the transport models described above represent processes that shape hillslopes in the Oregon Coast Range, we calibrated each model and simulated 500,000 yr of slope evolution to compare the resulting morphology with current landscape form. Thus, the assumption of approximate steady-state conditions (with a uniform erosion rate equal to 0.1 mm yr^{-1}) serves as a crucial cornerstone of this analysis. Given recent discoveries highlighting mechanisms by which portions of the Oregon Coast Range decidedly do not approximate steady-state erosion (Almond et al., 2007; Roering et al., 2005), we carefully chose the section of ridgeline and sideslopes used in this study (Fig. 5). Our intention is that the 200 × 360 m^2 patch of terrain shown in Figure 5B adequately represents the ubiquitous ridge and valley morphology of the Oregon Coast Range.

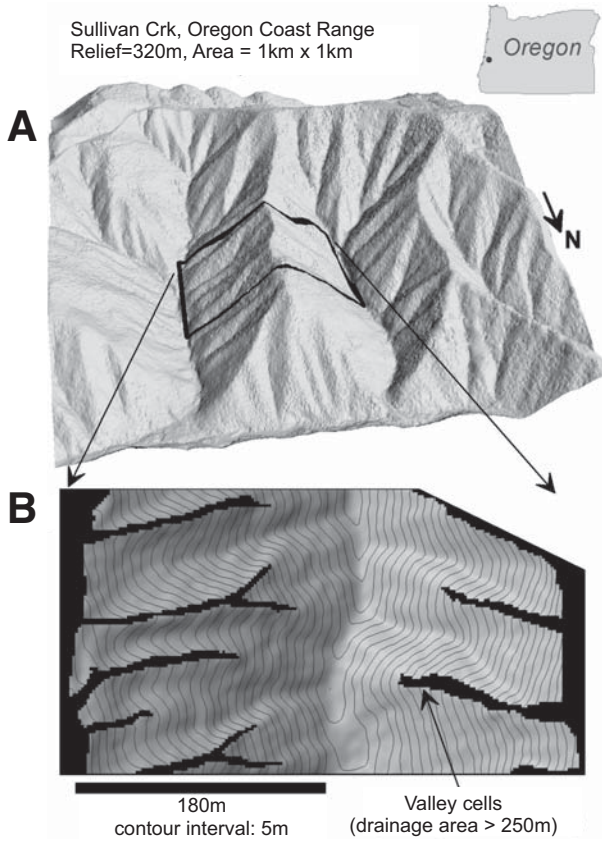

Figure 5. Location map (Lat = 43.464°, Long = −124.119°) of study site along Sullivan Creek, Oregon Coast Range. (A) Representative section of topography generated via airborne laser swath mapping (ALSM). (B) Perspective view of terrain used for the simulations in this study. Black cells represent valley nodes identified via a drainage area threshold and upon which boundary conditions are imposed.

Nonetheless, subtle, yet important characteristics of our site may influence the generality of our results. We chose the size of the study area based on the need to: (1) incorporate several ridge and valley sequences, and (2) retain computational efficiency.

High-resolution, gridded topographic data (with a 2 m grid spacing) for our site along Sullivan Creek, Oregon, reveal a pervasively pockmarked surface (Fig. 5A), which reflects the stochastic nature of bioturbation (such as pit and mound features created via tree turnover) as well as errors associated with the classification of vegetation and bare earth topographic points during airborne LiDAR data processing. Although the observed meter-scale roughness serves as the signature of interesting and relevant transport processes, here we recognize the transient nature of those features and instead focus our simulation results on the coarse-scale (>5 m) form that defines hillslopes. Consistent with previous studies, we represent episodic transport and production processes with a continuum approach.

Because the models discussed here do not apply to fluvial or debris flow processes that sculpt valleys and highly convergent, low-order portions of channel networks in the Oregon Coast Range (Stock and Dietrich, 2003), we only applied the mass conversation and transport equations to hillslope nodes of the topographic grid (Fig. 5B). We identified hillslope nodes by calculating the spatial distribution of drainage area (estimated with a fractional distribution method, e.g., Quinn et al., 1991) and specifying non-hillslope (or valley) points as having area greater than 250 m^2. This approach is consistent with geomorphic studies that use a drainage area-slope threshold to map channelization (Montgomery and Dietrich, 1992). We chose the 250 m^2 area threshold because this value causes the valley network to extend to the approximate location of mapped shallow landslides in topographic hollows within our study area (Montgomery et al., 2000). These landslides translated into debris flows and thus may reflect the spatial extent of processes that carve the upper tips of the drainage network. In the subsequent simulations, the background rate of base-level lowering (or rock uplift) is imposed on "valley" (or non-hillslope) cells, and the interior "hillslope" cells evolve as prescribed via the mass conservation, soil production and transport equations. We substituted each of the four transport models into Equation 2 and solved Equation 1 using an explicit, finite difference numerical model. Valley cells span the eastern and western margins of our study area, but the northern and southern margins are largely composed of hillslope cells (Fig. 5B). We thus specified boundary conditions of constant baselevel lowering at those locations.

We calibrated the four transport models by evolving the study area for 15,000 yr and determining the parameter values that generated a distribution of average erosion rates closest to the steady-state value of 0.1 mm yr^{-1}. We chose 15,000 yr for this calibration procedure because it was: (1) long enough to eradicate the meter-scale roughness associated with bioturbation and topographic data misclassification, and (2) short enough that identifiable coarser scale hillslope modification did not occur (Fernandes and Dietrich, 1997; Mudd and Furbish, 2007; Roering et al., 2001a). Using Equations 6, 7, 8, and 15, we varied values of K_1, K_2, K_3, and η (which is the coefficient of the depth-dependent expression for K_4), respectively, and calculated the root mean square error (RMSE) of the temporally averaged distribution of erosion rates (Equation 10 in Roering et al., 1999). For Equations 8 and 15, we used the previously calibrated S_c value of 1.25 (Roering et al., 1999). For Equation 15, we estimated the value of β by measuring the vertical variation of root density from more than 20 soil pits and landslide scars in the Oregon Coast Range (Gerber, 2004; Schmidt et al., 2001). Soil production (Equation 3) was simulated with parameters estimated at this study area by Heimsath et al. (2001b) (ε_0 = 0.268 mm yr^{-1}, μ = 3 m^{-1}, ρ_r = 2.0 g cm^{-3}, and ρ_s = 1.0 g cm^{-3}). Because soil depth is difficult to characterize across spatially extensive areas, we uniformly applied the mean soil depth (0.4 m) as the initial vertical soil depth in our simulations.

For the long-term simulations, we used the calibrated parameters and evolved the initial surface for 500,000 yr using the same boundary conditions and soil production parameters discussed above. This length of simulation time enables the slopes to completely adjust their coarse-scale morphology in accord with the specified transport models. We used morphologic criteria, such as gradient and curvature distributions and gradient-curvature plots (e.g., Fig. 4), to compare the results with the current topography and assess model performance. Comparing the visual appearance of the simulated landscapes with current topography also provides a useful and straightforward barometer of model predictions.

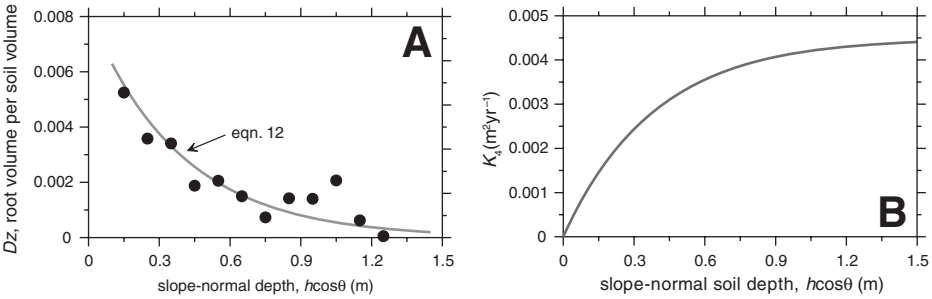

Figure 6. (A) Decline of root volume per unit soil volume with depth. Data points represent binned averages from 20+ observations from soil pits and landslide scarps in the Oregon Coast Range (Gerber, 2004; Schmidt et al., 2001). Gray curve represents Equation 12 fit to data where α = 0.0081 and β = 2.6 m^{-1} and r^2 = 0.63. (B) Variation of K_4 with normal soil depth (Equation 14) for η = 0.0045 m^2 yr^{-1} and β = 2.6 m^{-1}.

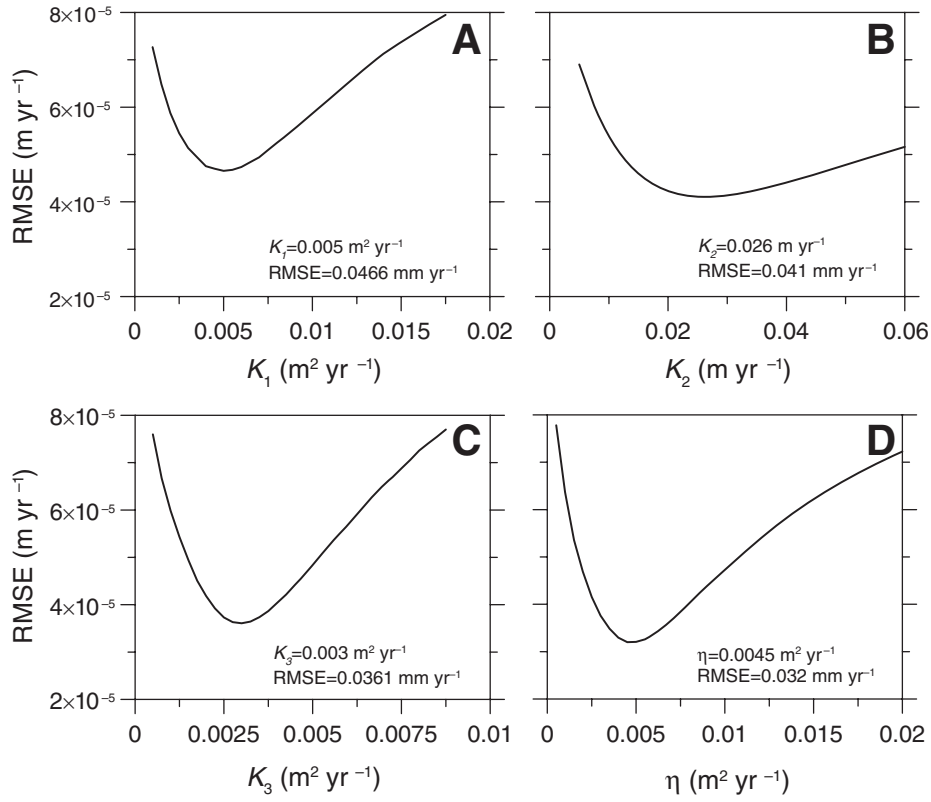

Figure 7. Root mean square error (RMSE) for modeled and steady-state erosion rates (0.1 mm yr^{-1}) as a function of coefficient values for the K_1, K_2, K_3, and K_4 (η) models (shown in A–D, respectively). Note that the K_4 model exhibits the lowest RMSE and thus best approximates the current landscape surface.

RESULTS

Model Calibration

Root data summarized from pits and landslide scars throughout the Oregon Coast Range indicate that the ratio of root volume to soil volume decreases exponentially with depth, consistent with previous studies (e.g., Jackson et al., 1996) (Fig. 6A). We fit Equation 12 to the root density profile data in Figure 6A, obtaining the parameter estimates α = 0.0081 and β = 2.6 m^{-1}. Interestingly, this β value is similar to Heimsath et al.'s (2001b) estimate of μ equal to 3 m^{-1}, which characterizes the exponential decay of soil production with depth. This rough correspondence suggests that tree root activity may be the dominant process driving soil production in the Oregon Coast Range.

For each of the four transport models, we simulated 15,000 yr of evolution for a range of parameter values (K_1, K_2, K_3, and η) and identified the parameter values associated with the lowest RMSE (Fig. 7). The nonlinear slope- and

depth-dependent model (K_4, which varies with η, S_c, and h) generated the lowest RMSE of 0.032 mm yr^{-1}, whereas the linear model (K_1) exhibited the largest RMSE of 0.047 mm yr^{-1}. Best-fit values for K_1, K_2, K_3, and η were determined to be 0.005 m^2 yr^{-1}, 0.026 m yr^{-1}, 0.003 m^2 yr^{-1}, and 0.0045 m^2 yr^{-1}, respectively. For the nonlinear slope- and depth-dependent model, the calibrated value of η enables us to estimate the variation of K_4 with soil depth. Figure 6B indicates that K_4 increases rapidly for thin soils and becomes effectively constant for soil depths greater than 1.2 m. In addition, this calibration allows us to estimate the sediment transport power per unit volume of disturbance agents (e.g., tree roots), P_v, by rearranging Equation 14 as $P_V = (\eta\beta g S_C^2 \rho\sigma)/(2\alpha) = 1.1$ J m^{-2} m^{-3} yr^{-1} (input parameters are summarized in Table 1).

Long-Term Simulations: Spatial Patterns

To evaluate our long-term (500,000 yr) model predictions, we constructed three-dimensional shaded relief images and gradient maps for comparison with the initial topography (Figs. 8A–8J). The current topography is distinguished by a relatively narrow north-south–trending ridge line, steep sideslopes (gradients between 0.8 and 1.0), and meter-scale noise associated with bioturbation and airborne laser swath mapping (ALSM) classification errors (Figs. 8A and 8F). The simulated landscapes (Figs. 8B–8E) exhibit much smoother surfaces, although each has a distinctive morphologic pattern driven by topography-transport feedbacks. In contrast to the current land surface, the linear model (K_1, Equation 6) generated a broadly curved ridgeline and locally steep hillslope-valley transitions (Figs. 8B and 8G). For this model, erosion scales with total curvature (equal to the sum of planform and profile curvature), which caused steep, subtly concave slopes above the tips of the channel network to develop high-profile convexity (and become extremely steep) to balance the absence of planform curvature (Fig. 8G). The depth-slope product model (K_2) also produced a broadly curved surface that poorly corresponds with the current morphology, although the hillslope-valley transitions were more gradual (Fig. 8H) than those for the K_1 model. Because fluxes can be accommodated by variations in soil depth as well as slope angle, the K_2 model produced a somewhat less convex but much gentler surface than the K_1 model. This outcome arises because downslope increases in steady-state soil depth (Equation 3) served to lessen downslope increases in gradient required to generate steady-state erosion. Importantly, neither of these models (K_1 or K_2) succeeds in preserving the narrow ridges and steep, nearly planar sideslopes characteristic of Oregon Coast Range slopes.

The nonlinear models (Equations 8 and 15) generated surfaces more consistent with the current form in that the primary ridgeline remained relatively sharp, and roughly planar slopes extended above the tips of the drainage network (Figs. 8I–8J). In addition, the distribution of hillslope gradients for these two models is roughly coincident with that for the current land surface because a large proportion of the study area and model surfaces exhibit slope gradients between 0.8 and 1.0 (Figs. 8F, 8I, and 8J) as represented by warm (yellow and orange) colors. The K_4 ridgeline is narrower than that for the K_3 model and better represents the initial morphology of our study site (Fig. 9A).

Interestingly, none of the models maintained the local sharpness (high convexity) of at least two small subsidiary ridges that trend west (to the right) in the central portion of our study area. The along-axis steepness of these isolated features elicited relatively rapid erosion and "rounding" during the simulations. These locally sharp features are not an areally extensive component of the study landscape, but their distinctive appearance warrants attention. Also, we observed a significantly broader distribution of soil depths for the K_1 model compared with more subdued soil depth variations for the other three models (Figs. 8K–8N). All of the models predicted relatively shallow soils along the ridgeline that became thicker downslope.

TABLE 1. PARAMETER DEFINITIONS AND VALUES

ρ_r, ρ_s = Rock and soil bulk density (gm cm^{*3})	2.0, 1.0**
ε_0 = Maximum soil production rate (mm yr^{*1})	0.268*
μ = Soil production exponential coefficient (m^{*1})	3.0*
E = Steady-state erosion rate (mm yr^{*1})	0.1*
E/ε_0 = Ratio of erosion rate to maximum soil production rate	0.37
K_1 = Transport coefficient (m^2 yr^{*1}), Equation 6	0.005
K_2 = Transport coefficient (m yr^{*1}), Equation 7	0.02
K_3 = Transport coefficient (m^2 yr^{*1}), Equation 8	0.003
S_c = Critical gradient, Equations 9 and 15	1.25**
α = Root density at the surface (m^3/m^3)	0.0081
B = Root density exponential decay term (m^{*1})	2.6
η = Transport coefficient (m^2 yr^{*1}), Equation 14	0.0045
P_v = Power per unit volume roots (J m^{*2} m^{*3} yr^{*1})	1.1

*(Heimsath et al., 2001b)
**(Roering et al., 1999)

Long-Term Simulations: Morphologic Signatures

Erosion rates averaged over each 500,000 yr simulation were variable for the different transport models (Figs. 9K–9N), but the distribution of erosion rates for the last 10,000 yr of each simulation was indistinguishable from 0.1 mm yr^{-1}, reflecting the attainment of steady-state conditions. At the conclusion of each simulation, we used quantitative representations of surface morphology to determine the extent to which the current landscape form was maintained. The current surface exhibits curvature values that become increasingly planar with steepness (see filled black circles in Fig. 9A) consistent with our one-dimensional, steady-state gradient-curvature analysis for the nonlinear slope-dependent transport models (see C_3^* and C_4^* curves in Fig. 4C). In contrast to the current morphology, the linear model (K_1) predicts that curvature values are independent of gradient (Fig. 9B). The depth-slope product model (K_2) predicts a slight decrease in convexity with gradient, which is consistent with our one-dimensional predictions (Fig. 4A), but inconsistent with our study site form (Fig. 9A). On gentle slopes, the K_1 and K_2 models predict curvature values significantly closer to zero than our observations for the current landscape (Figs. 9B and 9C).

The nonlinear slope-dependent models (K_3 and K_4) produced surfaces with gradient-curvature patterns similar to the current topography (Figs. 8D and 8E). The modeled surfaces exhibited negligible variability in curvature for low-gradient slopes (hilltops), whereas the current slopes have significant variation in curvature at these locations. Nonetheless, the trend expressed by the binned average gradient-curvature data (larger black circles) shows a "sigmoidal" pattern similar to the model predictions (Figs. 9D and 9E). Consistent with the initial morphology, both nonlinear models predicted a broad range of curvature values for slopes near the critical value, S_c. Notably, the K_4 (nonlinear slope- and depth-dependent) model better represents the current gradient-curvature pattern shown by the filled black circles in Figure 9A because it predicts higher convexity ridges ($\nabla^2 z = -0.078$ for $|\nabla z| = 0$) than does the K_3 model ($\nabla^2 z = -0.066$ for $|\nabla z| = 0$). As shown in Figures 8D and 8E, both nonlinear models produced ~300 points (~1% of the study area) with high convexity and steep slope angles ($|\nabla z| > 0.7$ and $\nabla^2 z < -0.05$). These points fall outside of the gradient-curvature pattern illustrated in our one-dimensional formulation

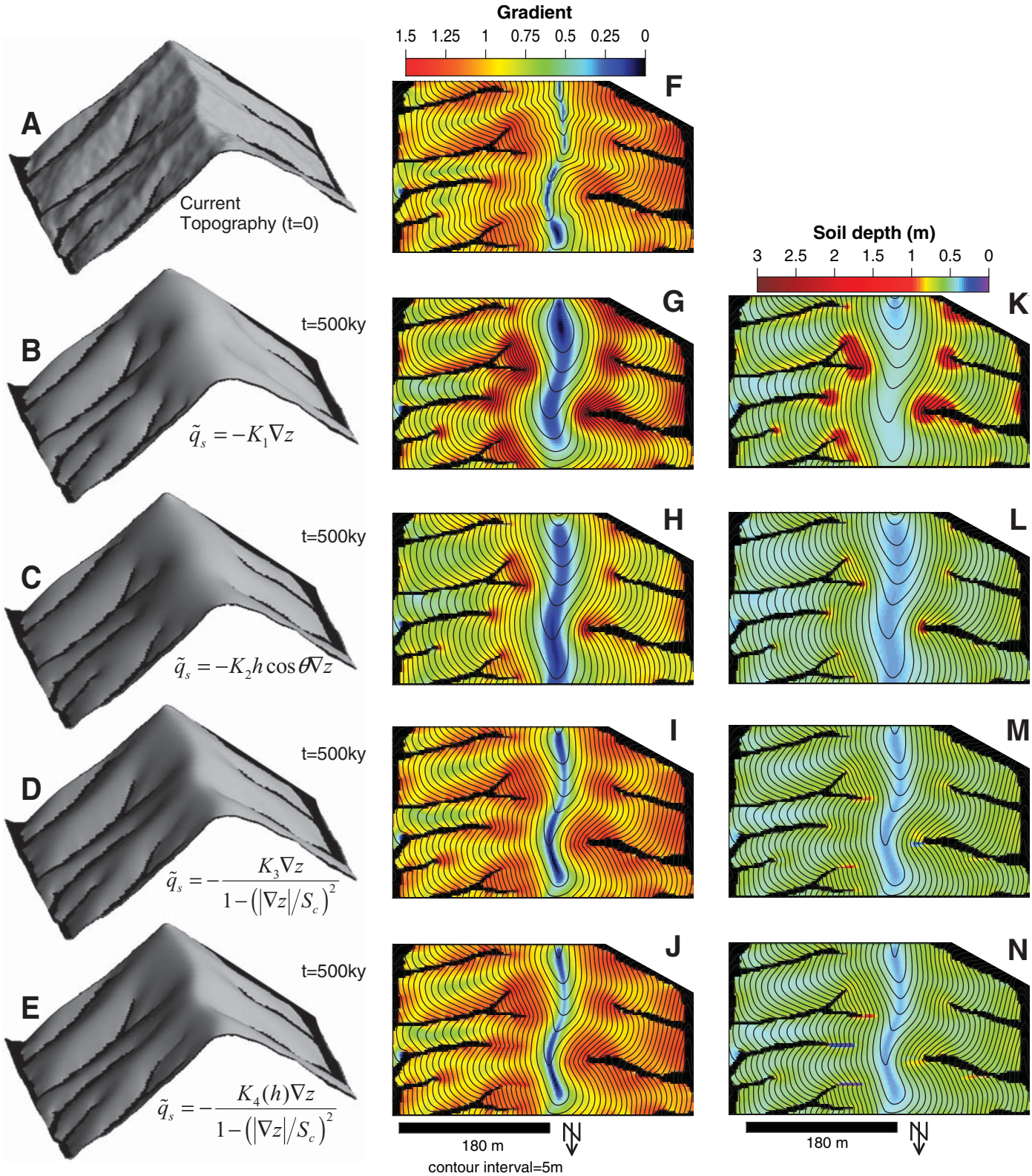

Figure 8. Comparison of simulation surfaces with current topography. (A–E) Perspective-view, shaded relief images of current and modeled topography. Modeled surfaces reflect 500,000 yr of evolution via the calibrated parameters given in Figure 7. (F–J) Spatial variation of hillslope gradient for current and modeled surfaces. The current surface is pockmarked due to bioturbation and data errors, whereas the modeled surfaces are uniformly smooth because of the continuum assumption used here. The nonlinear slope-dependent models (I and J) best represent the sharp, steep-sided slope morphology of the field site. (K–N) Spatial variation of simulated soil depth for the four transport models. Each model predicts thin soils near the ridge top and thicker soils along sideslopes.

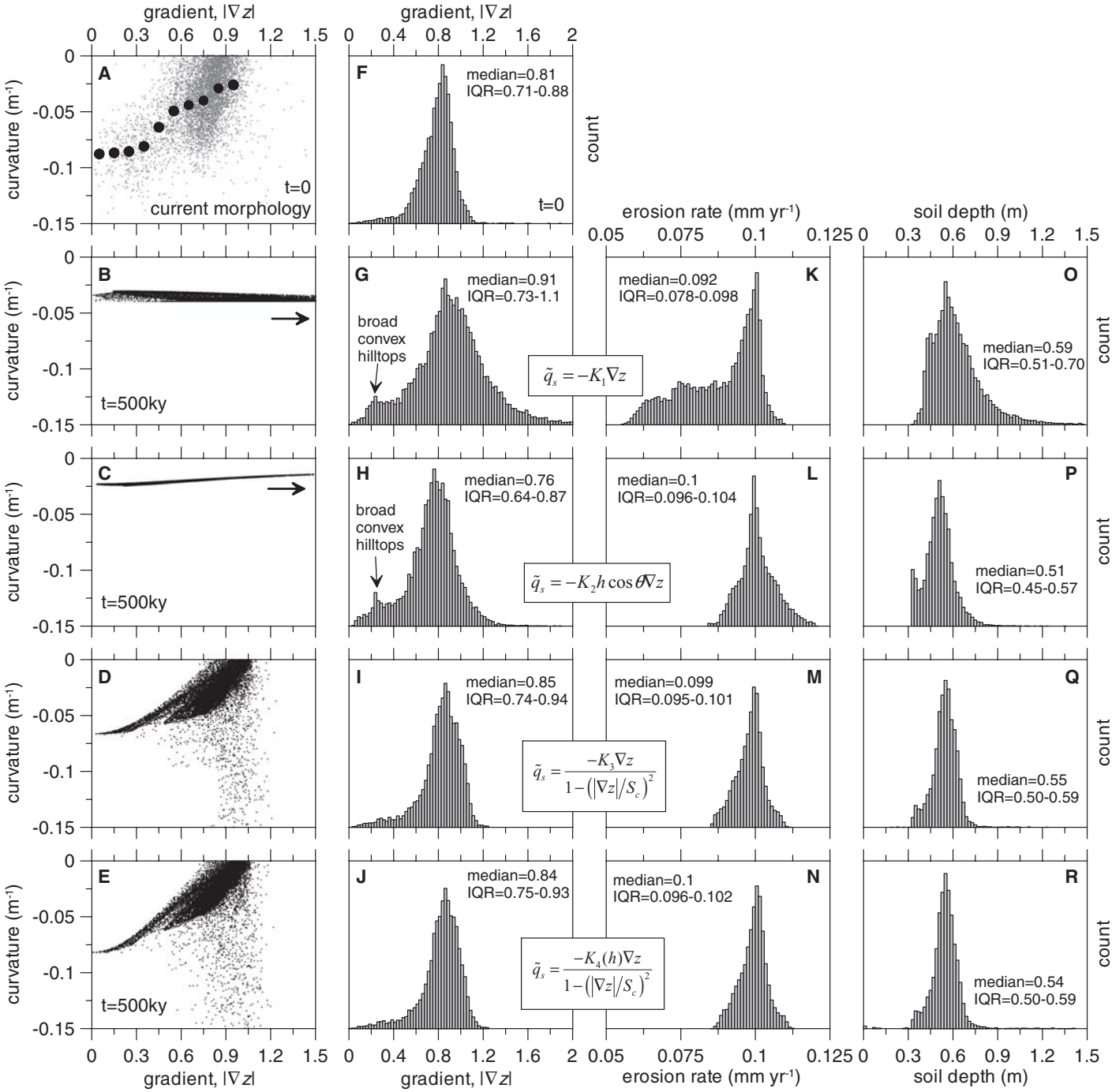

Figure 9. Comparison of gradient-curvature plots and distributions of gradient, erosion rate, and soil depth for current and modeled surfaces shown in Figure 8. (A–E) Variation of curvature with gradient for current and modeled surfaces. Only the nonlinear slope-dependent models (D and E) predict a substantial decrease in convexity with gradient, consistent with the current landscape. (F–J) Distributions of gradient for current and modeled surfaces. (K–N) Temporally averaged (500,000 yr) distributions of modeled erosion rates. (O–R) Distributions of soil depth for the modeled landscapes. The filled black circles in (A) represent binned average curvature values for our study site. While erosion rates averaged over the entire simulation (K–N) were variable, the distribution of erosion rates for the last 10,000 yr of each simulation was indistinguishable from 0.1 mm yr^{-1}.

(Fig. 4B) and correspond to cells immediately adjacent to the valley cells, such that they may be subject to boundary effects associated with our numerical analysis.

The distribution of gradient values and modeled erosion rates further distinguishes the transport model predictions (Figs. 9F–9J). In contrast to the current gradient distribution, the K_1 and K_2 models generated distributions with substantial concentrations of low-gradient values. These values correspond to the broadly curved, gentle ridgelines illustrated in Figures 8B and 8C. In particular, the K_1 model gradient distribution is characterized by a large interquartile range, whereas the other model distributions more closely reflect the magnitude of dispersion in the current gradient distribution. Slope angles for the K_2 model were somewhat gentler than the study site slopes, whereas distributions for the K_3 and K_4 models were difficult to distinguish from the current slope distribution. Temporally averaged erosion rates were also broadly distributed for the K_1 model (Fig. 9K) reflecting the long period of time some portions of the landscape required to attain the spatially constant, steady-state curvature value. In contrast, the other three models exhibited erosion rate distributions clustered around 0.1 mm yr^{-1} indicating their relatively rapid attainment of steady-state conditions (Figs. 8L–8N). The distribution of soil depth was also highly variable for the linear model (Fig. 8O) in comparison with the other models (Figs. 8P–8R). The median soil depth for all of the models was 0.5–0.6 m, consistent with field measurements, although the field-derived values exhibit greater variability driven by the stochastic nature of soil production processes (Heimsath et al., 2001b).

Morphologic Predictions of the Nonlinear Slope-Dependent Models

Although the two nonlinear slope-dependent models (K_3 and K_4) predict similar morphologic trends via the long-term simulation, the difference in predicted ridgetop convexity reveals an important distinction. The K_4 model better preserves the sharp ridgeline convexity that is characteristic of our study area. To clarify this difference in model behavior, we examined the first 50,000 yr of evolution for the two models and plotted the spatial distribution of average erosion rate (Figs. 10C and 10D). We chose 50,000 yr for this analysis because this length of time facilitates an initial phase of landform modification substantial enough to reveal differences between the two models. For steep and subtly concave slopes that occur just above the upper tips of the valley network, both models predict a similar erosion rate pattern with values generally lower than 0.1 mm yr^{-1} (shown by cool colors in Figs. 10C and 10D). The K_3 model, however, predicts rapid erosion rates (>0.15 mm yr^{-1}, shown by warm colors) for much of the high convexity terrain (e.g., ridges) in the study site. In contrast, hilltop erosion rates predicted with the K_4 model are more consistent with the background rate of 0.1 mm yr^{-1}. Distributions of average erosion rate for low-gradient ($|\nabla z|<0.4$) terrain during the first 50,000 yr reveals an abundance of rapidly eroding terrain for the K_3 model compared to the K_4 model (Figs. 10A and 10B). Because flux rates calculated with the K_4 model increase with soil depth and steady-state soil depth increases with slope angle (Equation 3), K_4-modeled slopes attain sharper hilltop convexity than when flux does not depend on soil depth (e.g., K_3 model).

DISCUSSION

The slope- and depth-dependent nonlinear transport (K_4) model proposed here (Equation 15) best preserved the topographic characteristics of our study site. In contrast to previous studies (Fernandes and Dietrich, 1997; Roering et al., 1999), our new formulation indicates that hilltop curvature for soil-mantled slopes varies nonlinearly with the steady-state erosion rate. According to our one-dimensional analysis of nonlinear depth- and slope-dependent transport (Equation 18d), steady-state hilltop

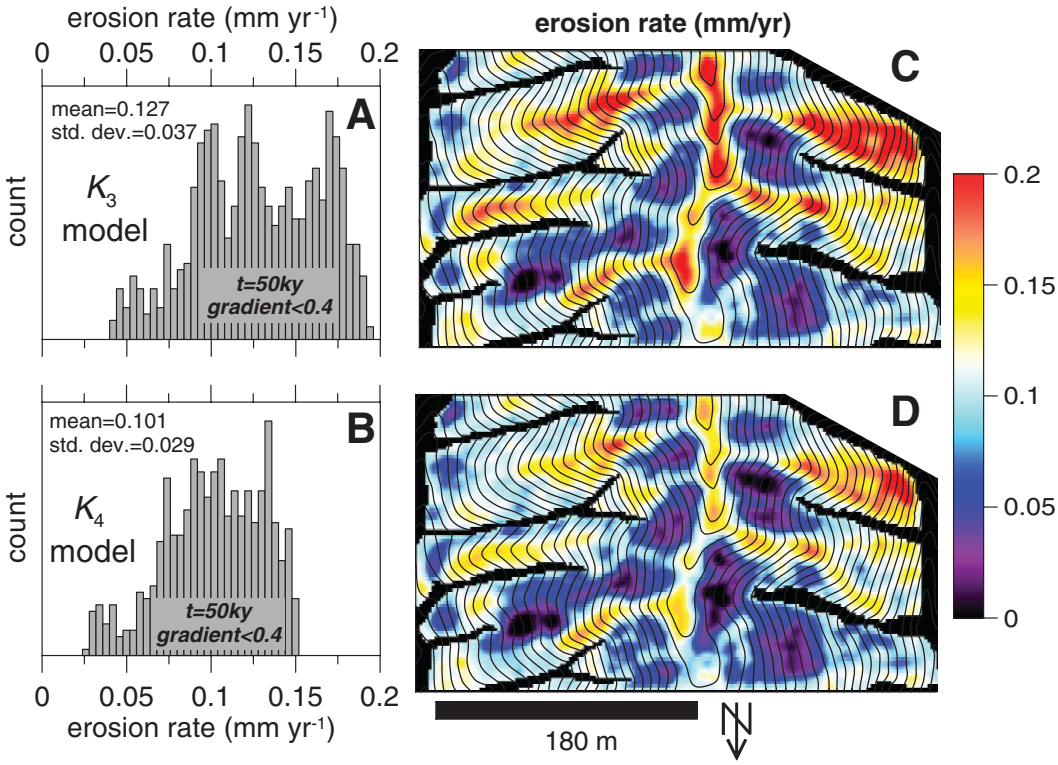

Figure 10. Comparison of spatial variations in erosion for the first 50,000 yr using the K_3 and K_4 models. (A–B) Distribution of erosion rates on terrain gentler than 0.4 predicted using the K_3 and K_4 models, respectively. The K_4 model predicts a narrower distribution that better corresponds with the steady-state erosion rate of 0.1 mm yr^{-1}. (C–D) Spatial variation of erosion rates after 50,000 yr of simulation time using the K_3 and K_4 models, respectively. The K_3 model predicts rapid erosion rates along the ridgelines, exceeding the steady-state value and reducing hilltop convexity.

curvature, $(d^2z/dx^2)_{HT}$, defined as the curvature where $dz/dx = 0$, is given by:

$$\left(\frac{d^2z}{dx^2}\right)_{HT} = \frac{-(\rho_r/\rho_s)(E/\eta)}{1-e^{(\beta/\mu)\ln(E/\varepsilon_0)}}. \quad (20a)$$

Equation 20a indicates that mapping erosion rate via hilltop convexity requires estimates of soil transport and production parameters. Using our calibrated parameters (Table 1), Equation 20a indicates that $(d^2z/dx^2)_{HT} = -0.078$, consistent with the results of our two-dimensional simulations (Fig. 9E). Dimensionless hilltop curvature (calculated as positive here to allow for plotting on a log scale) varies with erosion rate according to:

$$-C^*_{4(HT)} = \frac{1}{1-e^{(\beta/\mu)\ln(E/\varepsilon_0)}}. \quad (20b)$$

As $E/\varepsilon_0 \rightarrow 1$, the denominator of Equation 20b decreases rapidly and hilltops become exceedingly sharp (i.e., exhibit a narrow convexity) (Fig. 11). In essence, Equation 20b describes how hilltop convexity varies with E/ε_0 and β/μ in addition to proportional changes associated with E and η. Small changes in E/ε_0 can invoke large changes in $-C^*_{4(HT)}$ such that relative magnitudes of erosion rate (E) and the maximum soil production rate (ε_0) exert a strong control on slope morphology. Interestingly, this formulation indicates that the observed variability of hilltop convexity for natural slopes, which is substantial as shown in Figure 9A, may partly derive from small variations in processes and properties that influence soil production (as reflected in ε_0), including variations in lithology, weathering, and biogenic activity. For our study site, values of β and μ are of the same order ($\beta/\mu = 0.87$), suggesting that the depth-dependencies of soil production and soil transport processes may reflect the same suites of processes (e.g., tree turnover and root growth). As a result, we might expect that $\beta/\mu \approx 1$ in many field settings.

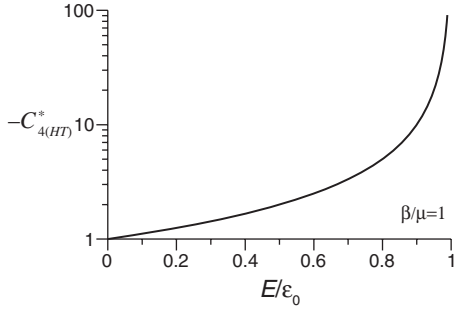

Figure 11. Variation of dimensionless hilltop curvature (denoted here as positive to facilitate plotting on a log scale) with E/ε_0 for a one-dimensional, steady-state solution of the K_4 model (Equation 20b). Dimensionless curvature increases rapidly as the steady-state erosion rate approaches the maximum soil production rate.

To explore the morphologic implications of landscapes wherein erosion rates approach the maximum soil production rate, we conducted a two-dimensional hillslope evolution simulation of our study site and imposed a baselevel lowering rate of 0.24 mm yr^{-1} such that $E/\varepsilon_0 = 0.9$. After 500,000 yr, the model hillslopes, which had attained a temporally invariant form, were steep with extremely sharp hilltops (Figs. 12A and 12B). Hillslope gradients (Fig. 12d) had a median value of 1.08 and more than 90% were steeper than 0.9 as low-gradient terrain became exceedingly sparse. Soil depths for the simulated landscape averaged 0.2 m and 90% of the landscape had soils thinner than 0.3 m. The gradient-curvature relationship for the modeled slopes (Fig. 12C) exhibited a convex-upward form, consistent with the results of our one-dimensional analysis for hillslopes with $E/\varepsilon_0 = 0.9$ (Fig. 4B). Hilltop curvature for this scenario is highly convex ($\nabla^2 z \approx -1.1$), reflecting the nonlinear dependency of E/ε_0 on hilltop morphology as predicted by Equation 20a, which predicts that $d^2z/dx^2_{HT} = -1.17$ when $E/\varepsilon_0 = 0.9$. This sharp-crested model morphology arises because soil depths are shallow, such that hilltops must develop high convexity to accommodate rapid erosion. On sideslopes, by contrast, the nonlinear slope-dependency on transport rates enables the base-level lowering rate to be accommodated with modest increases in slope angle. This simulation may be relevant to many natural settings, including the steep, sharp-crested, and thin soil-mantled Verdugo Hills described by Strahler (1950). In addition, other portions of the San Gabriel Mountains experiencing rapid uplift exhibit extremely sharp hilltops and thin (and likely tenuous) soil mantles (Whipple et al., 2005), consistent with our conceptualization. Similarly, Young (1961) describes sensitive feedbacks between soil thickness and slope angle for catchments in Wales such that soils become thin and patchy as slope angles approach 45°–50°.

Significant uncertainty accompanies the estimation of topographic derivatives used to distinguish our model predictions (Figs. 9B–9C). For example, fractional standard error estimates for curvature values (error bars are not shown in our plots to improve clarity) range from 20% to 50%. As a result, data sets based on small sample sizes may compromise the diagnostic ability of gradient-curvature plots for distinguishing hillslope transport models. In contrast, our morphologic observations of natural slopes incorporate >19,000 data points and show consistent patterns in gradient-curvature space as defined via spatially extensive data. Our approach averages the morphologic characteristics of numerous hillslopes, reinforcing the systematic nature of gradient-curvature trends.

Our assessment of model performance depends on the assumption of steady-state hillslope erosion for our Oregon Coast Range study site. Certainly, large landsliding, drainage capture, differential incision driven by resistant mafic dikes, and lateral bedrock channel migration, conspire in various locales of the Oregon Coast Range to impose erosion rates significantly higher or lower than the assumed 0.1 mm yr^{-1} used here (Almond et al., 2007; Baldwin and Howell, 1949; Kobor and Roering, 2004; Moeller, 1990; Personius, 1995; Roering et al., 2005). Fortunately, the topographic manifestation of these processes is significant and readily identifiable via visual inspection or digital elevation model (DEM) analysis. In the late 1980s, the study site used here was chosen for extensive hydrologic study (Anderson and Dietrich, 2001; Montgomery et al., 1997; Torres et al., 1998) because of its collection of characteristic ridge and valley sequences (Montgomery and Dietrich, 1989). Although at least two of the models presented above generate morphologic patterns similar to the current land surface, we cannot rule out the possibility that transient adjustments are manifest. Given the ubiquity of erosion rates between 0.05 and 0.2 mm yr^{-1} observed in characteristic ridge and valley terrain of the Oregon Coast Range (Bierman et al., 2001; Heimsath et al., 2001b; Reneau and Dietrich, 1991), the magnitude of associated deviations in morphologic trends should not significantly hamper our ability to compare and differentiate model behavior. Nonetheless, a more spatially extensive testing of our calibrated equations should be conducted, including areas that appear to show decidedly non-steady morphologic features.

Perhaps the most readily observed result of our simulations is that meter-scale topographic "noise" ubiquitous across the current landscape gives way to smooth modeled land surfaces (Figs. 8A–8E). Using a wavelet-based analysis of variations in the dispersion of local curvature, Lashermes et al. (2007) demonstrated that the length scale at which topography becomes "noisy" in the Oregon Coast Range is ~10 m. Below this length scale, pit and mound features associated with tree turnover and other forms of bioturbation dominate the topography. Misclassification of the ALSM data may also contribute to this meter-scale topographic roughness. At length scales greater than 10 m, the

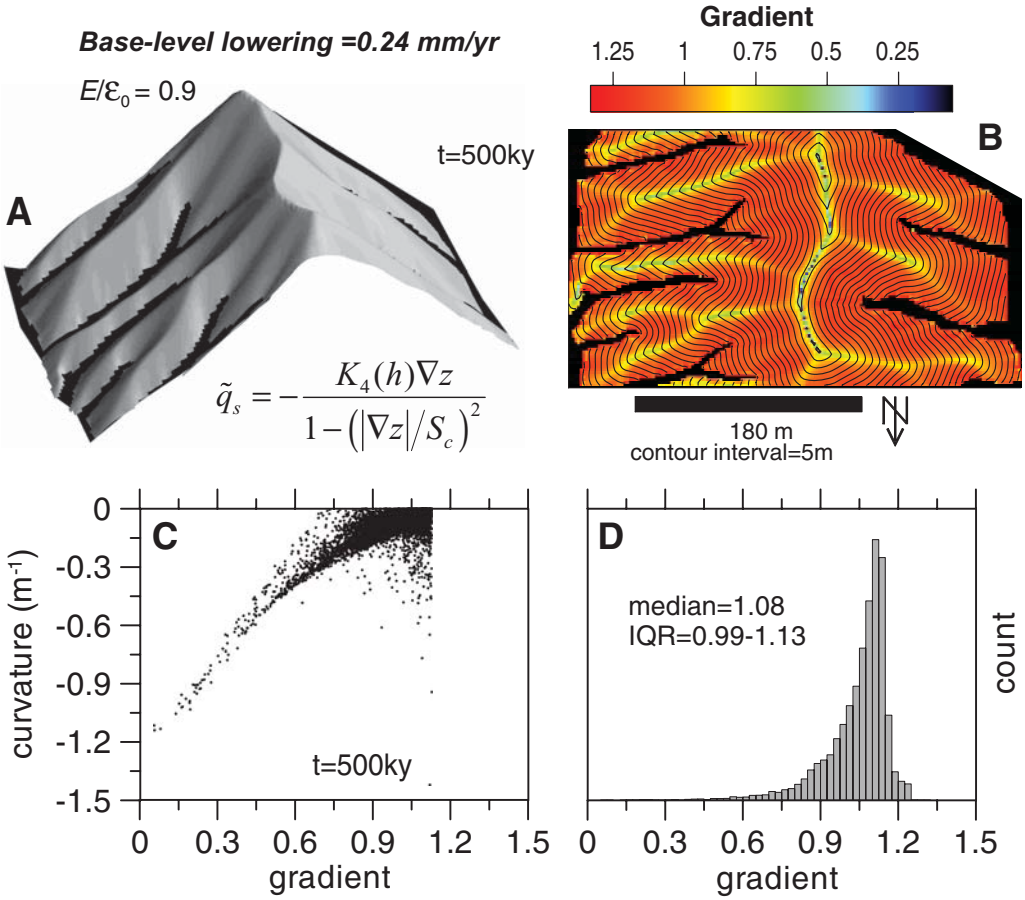

Figure 12. Summary of simulation results of the K_4 model after 500,000 yr with a base-level lowering rate of 0.24 mm yr^{-1}, such that E/ε_0 = 0.9. (A) Perspective shaded relief image (compare to current surface shown in Fig. 8A); (B) spatial variation of modeled gradient, and (C) variation of curvature with gradient. Note that the convex upward gradient-curvature pattern is consistent with our analytical, one-dimensional solution shown in Figure 4B. (D) Distribution of hillslope gradient for the modeled surface.

morphologic signature of hillslopes and valleys predominates. Because our simulations do not account for the stochasticity of biogenic-driven transport processes or episodic fire-driven transport (Roering and Gerber, 2005), our simulated slopes do not exhibit meter-scale roughness but instead average across these temporal variations in flux. Future studies should explicitly account for statistical variations in flux associated with natural processes.

Traditionally, the erosion of concave terrain has been associated with advective processes such as overland flow erosion (e.g., Smith and Bretherton, 1972). As noted by Dietrich et al. (2003), nonlinear slope-dependent models (e.g., Equations 8 and 15) can accommodate landscape lowering for steep, slightly concave slopes. In our simulations, steep slopes perched above the upper tips of the valley networks exhibit concavity yet experience erosion, consistent with that assertion. The nonlinearity of the transport relationships facilitate this behavior as erosion is a complex combination of planform and profile gradient and curvature values scaled by the degree to which the nonlinearity affects transport rates (Equation 9 in Roering et al., 1999). To avoid confusion, we constructed our gradient-curvature plots to only show planar or convex terrain, although the simulations for the K_3 and K_4 models did generate slopes with slight concavity that accounted for <15% of the study area. The linear and depth-slope product models (Equations 6 and 7) are unable to generate concave terrain that experiences erosion.

Analogous to the analysis by Yoo et al. (2005), we use our analysis of erosion and transport rates to estimate power per unit volume of biota, P_V. By assuming that gopher-driven soil transport at their California field site and documenting how gopher density varies with soil depth, Yoo et al. (2005) calculated how flux rates adjust to climate-driven perturbations in gopher population density, enabling an explicit linkage between geomorphic processes and ecology. Our calibration of the K_4 model (Equation 14) assumes that bioturbation associated with root action (e.g., growth, dilation, or tree turnover) dominates transport in the Oregon Coast Range, which is a reasonable assumption given the high frictional strength of the coarse colluvial soils (Schmidt et al., 2001). Nonetheless, additional disturbance mechanisms, such as mammal burrowing, may contribute to soil mobilization and displacement but are not incorporated here. Although our new nonlinear model (Equation 15) has three parameters (whereas the previous nonlinear model has only two), β can be estimated via field-based data and thus is not a "fit" parameter.

Our delineation of the valley network does not correspond to the location of channels with definable banks but instead accounts for the upstream extent of valley sculpting via shallow landslides that trigger debris flows (Stock and Dietrich, 2006). The location of shallow landslide initiation likely varies temporally according to climatic and vegetation changes (Reneau and Dietrich, 1990), however, and as a result we acknowledge that other drainage area threshold values are defensible. Our area threshold (250 m^2), however, is consistent with the value of drainage area per unit contour (a/b = 57 m, where b = 4 m) that defines the hillslope-channel transition at this site (Roering et al., 1999) and thus may reflect the effective long-term average extent of valley-sculpting processes.

Our analysis highlights the importance of soil depth in modulating process-scale morphology in soil-mantled landscapes. Anderson (2002) reasoned that transport rates should depend on the depth of available soil and developed a freeze-thaw model whereby flux rates attained a

maximum value for soils greater than the depth of frost penetration. Our approach here is analogous and is also consistent with a rate-process–based approach that also accounts for the depth of disturbance penetration in estimating net flux (Roering, 2004). Feedbacks between ecological processes and soil depth are important to consider, but are beyond the scope of this contribution. For example, moisture and nutrient constraints may favor a different assemblage of flora and fauna, if soils thin below a particular depth, affecting the magnitude and depth-dependency of transport. In the absence of soil, additional processes not addressed in this contribution (such as rockfall) likely ensue. In contrast to the depth-slope product model (Equation 7), our proposed model (Equation 14) explicitly accounts for how the distribution of transport agents varies with soil depth. Our formulation thus avoids the problematic scenario for which the depth-slope product model predicts proportional increases in flux as soils become inordinately thick (i.e., much thicker than the depth along which transporting agents act).

CONCLUSIONS

Our results constitute the first comprehensive, two-dimensional evaluation of soil transport models for a real landscape. Our findings highlight the critical role of soil depth in modulating hillslope processes and landscape form. Because soil production processes act in a slope-normal orientation, steady-state soil depth increases with slope angle, such that soils are thinnest along hilltops. In our proposed nonlinear slope- and depth-dependent model, flux rates increase with the depth of available soil according to an exponential function describing how the density of transport-inducing biota varies with depth. This formulation stipulates that transport rates attain a maximum value for depths greater than the deepest extent of bioturbation. We tested four representative transport models and used a one-dimensional, steady-state solution for each to show that gradient-curvature plots should serve as useful tools for differentiating model behavior. We calibrated each model by simulating 15,000 yr of evolution across our Oregon Coast Range study site and determining parameter values that generated the smallest average deviation from the steady-state erosion rate of 0.1 mm yr^{-1}. For our proposed nonlinear slope- and depth-dependent model, we used field-based data summarizing the distribution of transport-inducing tree roots to calibrate the model. After simulating 500,000 yr of slope evolution using the calibrated parameters for each model, we used three-dimensional representations of the current and modeled surfaces, as well as gradient and curvature distributions, to assess model performance. The two models for which flux varies linearly with slope gradient generated broad, convex hilltops inconsistent with the current study site morphology. The two nonlinear slope-dependent models predicted slopes along which curvature values became increasingly planar with steepness. The proposed nonlinear slope- and depth-dependent model best preserved the sharp, narrow hilltops and steep nearly planar sideslopes characteristic of our study site. Our new formulation predicts that steady-state hilltop convexity varies nonlinearly with erosion rate such that as erosion rates approach the maximum soil production rate, hilltops become exceedingly sharp.

ACKNOWLEDGMENTS

The author was supported by National Science Foundation grant EAR-0309975. Discussions with Bill Dietrich and Simon Mudd greatly improved the manuscript. Reviews by Jon Pelletier and Arjun Heimsath sharpened the manuscript and were highly appreciated.

REFERENCES CITED

Ahnert, F., 1970a, A comparison of theoretical slope models with slopes in the field: Zeitschrift fur Geomorphologie, v. 9, p. 88–101.

Ahnert, F., 1970b, Functional relationships between denudation, relief and uplift in large, mid-latitude drainage basins: American Journal of Science, v. 268, p. 243–263.

Ahnert, F., 1976, Brief description of a comprehensive three-dimensional process-response model of landform development: Zeitschrift fur Geomorphologie, v. 25, Supplement, p. 29–49.

Ahnert, F., 1984, Local relief and the height limits of mountain ranges: American Journal of Science, v. 284, p. 1035–1055.

Almond, P., Roering, J.J., and Hales, T.C., 2007, Using soil residence time to delineate spatial and temporal patterns of landscape disequilibrium: Journal of Geophysical Research, v. 112, F03S17, doi: 10.1029/2006JF000568

Anderson, R.S., 1994, Evolution of the Santa Cruz Mountains, California, through tectonic growth and geomorphic decay: Journal of Geophysical Research, v. 99, p. 20,161–20,174, doi: 10.1029/94JB00713.

Anderson, R.S., 2002, Modeling the tor-dotted crests, bedrock edges, and parabolic profiles of high alpine surfaces of the Wind River Range, Wyoming: Geomorphology, v. 46, p. 35–58, doi: 10.1016/S0169-555X(02)00053-3.

Anderson, R.S., and Humphrey, N.F., 1989, Interaction of weathering and transport processes in the evolution of arid landscapes, *in* Cross, T.A., ed., Quantitative dynamic stratigraphy: Englewood Cliffs, New Jersey, Prentice Hall, p. 349–361.

Anderson, S.P., and Dietrich, W.E., 2001, Chemical weathering and runoff chemistry in a steep headwater catchment: Hydrological Processes, v. 15, p. 1791–1815, doi: 10.1002/hyp.240.

Andrews, D.J., and Bucknam, R.C., 1987, Fitting degradation of shoreline scarps by a nonlinear diffusion model: Journal of Geophysical Research, v. 92, p. 12,857–12,867.

Arrowsmith, J.R., Pollard, D.D., and Rhodes, D.D., 1996, Hillslope development in areas of active tectonics: Journal of Geophysical Research, v. 101, p. 6255–6275, doi: 10.1029/95JB02583.

Avouac, J.-P., and Peltzer, G., 1993, Active tectonics in southern Xinjiang, China: Analysis of terrace riser and normal fault scarp degradation along the Hotan-Qira fault system: Journal of Geophysical Research, v. 98, p. 21,773–21,807.

Baldwin, E.M., 1956, Geologic map of the lower Siuslaw River area, Oregon: U.S. Geological Survey Oil and Gas Investigations Map OM-186.

Baldwin, E.M., and Howell, P.W., 1949, The Long Tom, a former tributary of the Siuslaw River: Northwest Science, v. 23, p. 112–124.

Benda, L., and Dunne, T., 1997, Stochastic forcing of sediment supply to channel networks from landsliding and debris flow: Water Resources Research, v. 33, p. 2849–2863, doi: 10.1029/97WR02388.

Beschta, R.L., 1978, Long-term patterns of sediment production following road construction and logging in the Oregon Coast Range: Water Resources Research, v. 14, p. 1011–1016.

Bierman, P., Clapp, E., Nichols, K., Gillespie, A., and Caffee, M., 2001, Using cosmogenic nuclide measurements in sediments to understand background rates of erosion and sediment transport, *in* Harmon, R.S., and Doe, W.M., eds., Landscape erosion and evolution modeling: New York, Kluwer Academic Plenum, p. 89–115.

Braun, J., and Sambridge, M., 1997, Modelling landscape evolution on geological time scales: A new method based on irregular spatial discretization: Basin Research, v. 9, p. 27–52, doi: 10.1046/j.1365-2117.1997.00030.x.

Braun, J., Heimsath, A.M., and Chappell, J., 2001, Sediment transport mechanisms on soil-mantled hillslopes: Geology, v. 29, p. 683–686, doi: 10.1130/0091-7613(2001)029<0683:STMOSM>2.0.CO;2.

Burbank, D.W., Leland, J., Fielding, E., Anderson, R.S., Brozovic, N., Reid, M.R., and Duncan, C., 1996, Bedrock incision, rock uplift and threshold hillslopes in the Northwestern Himalayas: Nature, v. 379, p. 505–510, doi: 10.1038/379505a0.

Canadell, J., Jackson, R.B., Ehleringer, J.R., Mooney, H.A., Sala, O.E., and Schulze, E.D., 1996, Maximum rooting depth of vegetation types at the global scale: Oecologia, v. 108, p. 583–595, doi: 10.1007/BF00329030.

Carson, M.A., and Petley, D.J., 1970, The existence of threshold hillslopes in the denudation of the landscape: Transactions of the Institute of British Geographers, no. 49, p. 71–95, doi: 10.2307/621642.

Chan, M.A., and Dott, J., R.H., 1983, Shelf and deep-sea sedimentation in Eocene forearc basin, western Oregon-fan or non-fan?: American Association of Petroleum Geologists Bulletin, v. 67, p. 2100–2116.

Culling, W.E.H., 1960, Analytical theory of erosion: The Journal of Geology, v. 68, p. 336–344.

Culling, W.E.H., 1963, Soil creep and the development of hillside slopes: The Journal of Geology, v. 71, p. 127–161.

Davis, W.M., 1892, The convex profile of badland divides: Science, v. 20, p. 245, doi: 10.1126/science.ns-20.508.245.

Dietrich, W.E., and Dunne, T., 1978, Sediment budget for a small catchment in mountainous terrain: Zeitschrift fur Geomorphologie, v. 29, Supplement, p. 191–206.

Dietrich, W.E., and Perron, J.T., 2006, The search for a topographic signature of life: Nature, v. 439, p. 411–418, doi: 10.1038/nature04452.

Dietrich, W.E., Bellugi, D., Sklar, L.S., Stock, J.D., Heimsath, A.M., and Roering, J.J., 2003, Geomorphic transport laws for predicting landscape form and dynamics, *in* Iverson, R.M., and Wilcock, P., eds., Prediction in geomorphology: Washington, D.C., American Geophysical Union, p. 103–132.

Fernandes, N.F., and Dietrich, W.E., 1997, Hillslope evolution by diffusive processes: The timescale for equilibrium adjustments: Water Resources Research, v. 33, p. 1307–1318, doi: 10.1029/97WR00534.

Furbish, D.J., and Fagherazzi, S., 2001, Stability of creeping soil and implications for hillslope evolution: Water Resources Research, v. 37, p. 2607–2618, doi: 10.1029/2001WR000239.

Gabet, E.J., 2000, Gopher bioturbation: Field evidence for nonlinear hillslope diffusion: Earth Surface Processes and Landforms, v. 25, p. 1419–1428, doi: 10.1002/1096-9837(200012)25:13<1419::AID-ESP148>3.0.CO;2-1.

Gabet, E.J., Reichman, O.J., and Seabloom, E.W., 2003, The effects of bioturbation on soil processes and sediment transport: Annual Review of Earth and Planetary Sciences, v. 31, p. 249–273.

Gerber, M., 2004, Geomorphic response to wildfire in the Oregon Coast Range [M.S. thesis]: Eugene, Oregon, University of Oregon.

Gilbert, G.K., 1877, Report on the geology of the Henry Mountains (Utah): Washington, D.C., U.S. Geographical and Geological Survey of the Rocky Mountain Region, Government Printing Office, 160 p.

Gilbert, G.K., 1909, The convexity of hilltops: The Journal of Geology, v. 17, p. 344–350.

Hanks, T.C., 2000, The age of scarplike landforms from diffusion-Equation analysis, *in* Noller, J.S., Sower, J.M., and Lettis, W.M., eds., Quaternary geochronology, methods and applications: Washington, D.C., American Geophysical Union, p. 313–338.

Heimsath, A.M., Chappell, J., Dietrich, W.E., Nishiizumi, K., and Finkel, R.C., 2001a, Late Quaternary erosion in southeastern Australia: A field example using cosmogenic nuclides: Quaternary International, v. 83–85, p. 169–185, doi: 10.1016/S1040-6182(01)00038-6.

Heimsath, A.M., Dietrich, W.E., Nishiizumi, K., and Finkel, R.C., 2001b, Stochastic processes of soil production and transport: Erosion rates, topographic variation and cosmogenic nuclides in the Oregon Coast Range: Earth Surface Processes and Landforms, v. 26, p. 531–552, doi: 10.1002/esp.209.

Heimsath, A.M., Chappell, J., Spooner, N.A., and Questiaux, D.G., 2002, Creeping soil: Geology, v. 30, p. 111–114, doi: 10.1130/0091-7613(2002)030<0111:CS>2.0.CO;2.

Heimsath, A.M., Furbish, D.J., and Dietrich, W.E., 2005, The illusion of diffusion: Field evidence for depth-dependent sediment transport: Geology, v. 33, p. 949–952, doi: 10.1130/G21868.1.

Heller, P.L., and Dickinson, W.R., 1985, Submarine ramp facies model for delta-fed, sand-rich turbidite systems: American Association of Petroleum Geologists Bulletin, v. 69, p. 960–976.

Herman, F., and Braun, J., 2006, A parametric study of soil transport mechanisms, *in* Willett, S.D., Hovius, N., Brandon, M.T., and Fisher, D.M., eds., Tectonics, climate, and landscape evolution: Boulder, Colorado, Geological Society of America Special Paper 398, Penrose Conference Series, p. 191–200.

Howard, A.D., 1994, A detachment-limited model of drainage basin evolution: Water Resources Research, v. 30, p. 2261–2285, doi: 10.1029/94WR00757.

Howard, A.D., 1997, Badland morphology and evolution: Interpretation using a simulation model: Earth Surface Processes and Landforms, v. 22, p. 211–227, doi: 10.1002/(SICI)1096-9837(199703)22:3<211::AID-ESP749>3.0.CO;2-E.

Istanbulluoglu, E., Tarboton, D.G., Pack, R.T., and Luce, C.H., 2004, Modeling of the interactions between forest vegetation, disturbances, and sediment yields: Journal of Geophysical Research, v. 109, F01009.

Jackson, R.B., Canadell, J., Ehleringer, J.R., Mooney, H.A., Sala, O.E., and Schulze, E.D., 1996, A global analysis of root distributions for terrestrial biomes: Oecologia, v. 108, p. 389–411, doi: 10.1007/BF00333714.

Kelsey, H.M., Ticknor, R.L., Bockheim, J.G., and Mitchell, C.E., 1996, Quaternary upper plate deformation in coastal Oregon: Geological Society of America Bulletin, v. 108, p. 843–860, doi: 10.1130/0016-7606(1996)108<0843:QUPDIC>2.3.CO;2.

Kirkby, M.J., 1971, Hillslope process-response models based on the continuity equation: Institute of British Geographers, Special Publication, v. 3, p. 15–30.

Kirkby, M.J., 1984, Modelling cliff development in South Wales: Savigear re-reviewed: Zeitschrift fur Geomorphologie, v. 28, p. 405–426.

Kobor, J.S., and Roering, J.J., 2004, Systematic variation of bedrock channel gradients in the central Oregon Coast Range: Implications for rock uplift and shallow landsliding: Geomorphology, v. 62, p. 239–256.

Kooi, H., and Beaumont, C., 1994, Escarpment evolution on high-elevation rifted margins: Insights derived from a surface processes model that combines diffusion, advection, and reaction: Journal of Geophysical Research, v. 99, p. 12,191–12,209, doi: 10.1029/94JB00047.

Koons, P.O., 1989, The topographic evolution of collisional mountain belts: A numerical look at the Southern Alps, New Zealand: American Journal of Science, v. 289, p. 1041–1069.

Lashermes, B., Foufoula-Georgiou, E., and Dietrich, W., Channel network extraction from high resolution topography using wavelets: Geophysical Research Letters, v. 34, L23S04, doi: 10.1029/2007Gl031140.

Lovell, J.P.B., 1969, Tyee Formation: Undeformed turbidites and their lateral equivalents: Mineralogy and paleogeography: Geological Society of America Bulletin, v. 80, p. 9–22, doi: 10.1130/0016-7606(1969)80[9:TFUTAT]2.0.CO;2.

McNeill, L.C., Goldfinger, C., Kulm, L.D., and Yeats, R.S., 2000, Tectonics of the Neogene Cascadia forearc basin: Investigations of a deformed late Miocene unconformity: Geological Society of America Bulletin, v. 112, p. 1209–1224, doi: 10.1130/0016-7606(2000)112<1209:TOTNCF>2.3.CO;2.

Minasny, B., and McBratney, A.B., 2006, Mechanistic soil-landscape modelling as an approach to developing pedogenetic classifications: Geoderma, v. 133, p. 138–149, doi: 10.1016/j.geoderma.2006.03.042.

Mitchell, C.E., Vincent, P., Weldon, R.J., and Richards, M., 1994, Present-day vertical deformation of the Cascadia margin, Pacific Northwest, United States: Journal of Geophysical Research, v. 99, p. 12,257–12,277, doi: 10.1029/94JB00279.

Moeller, B., 1990, Stream capture in the Central Oregon Coast Range and its relationship to tectonic and structural geology: Eugene, Oregon, University of Oregon.

Montgomery, D.R., 2001, Slope distributions, threshold hillslopes, and steady-state topography: American Journal of Science, v. 301, p. 432–454, doi: 10.2475/ajs.301.4-5.432.

Montgomery, D.R., and Brandon, M.T., 2002, Topographic controls on erosion rates in tectonically active mountain ranges: Earth and Planetary Science Letters, v. 201, p. 481–489, doi: 10.1016/S0012-821X(02)00725-2.

Montgomery, D.R., and Dietrich, W.E., 1989, Source areas, drainage density, and channel initiation: Water Resources Research, v. 25, p. 1907–1918.

Montgomery, D.R., and Dietrich, W.E., 1992, Channel initiation and the problem of landscape scale: Science, v. 255, p. 826–830, doi: 10.1126/science.255.5046.826.

Montgomery, D.R., Dietrich, W.E., Torres, R., Anderson, S.P., Heffner, J.T., and Loague, K., 1997, Hydrologic response of a steep, unchanneled valley to natural and applied rainfall: Water Resources Research, v. 33, p. 91–109, doi: 10.1029/96WR02985.

Montgomery, D.R., Schmidt, K.M., Greenberg, H., and Dietrich, W.E., 2000, Forest clearing and regional landsliding: Geology, v. 28, p. 311–314, doi: 10.1130/0091-7613(2000)28<311:FCARL>2.0.CO;2.

Mudd, S.M., and Furbish, D.J., 2007, Responses of soil-mantled hillslopes to transient channel incision rates: Journal of Geophysical Research, v. 112, article no. F03S18.

Orr, E.L., Orr, W.N., and Baldwin, E.M., 1992, Geology of Oregon: Dubuque, Kendall/Hunt, 254 p.

Penck, W., 1953, Morphological analysis of landforms: London, Macmillan, 429 p.

Personius, S.F., 1995, Late Quaternary stream incision and uplift in the forearc of the Cascadia subduction zone, western Oregon: Journal of Geophysical Research, v. 100, p. 20,193–20,210, doi: 10.1029/95JB01684.

Quinn, P., Beven, K., Chevallier, P., and Planchon, O., 1991, The prediction of hillslope flow paths for distributed hydrological modeling using digital terrain models: Hydrological Processes, v. 5, p. 59–80, doi: 10.1002/hyp.3360050106.

Reneau, S.L., and Dietrich, W.E., 1990, Depositional history of hollows on steep hillslopes, coastal Oregon and Washington: National Geographic Research, v. 6, p. 220–230.

Reneau, S.L., and Dietrich, W.E., 1991, Erosion rates in the Southern Oregon Coast Range: Evidence for an equilibrium between hillslope erosion and sediment yield: Earth Surface Processes and Landforms, v. 16, p. 307–322, doi: 10.1002/esp.3290160405.

Roering, J., 2004, Soil creep and convex-upward velocity profiles: Theoretical and experimental investigation of disturbance-driven sediment transport on hillslopes: Earth Surface Processes and Landforms, v. 29, p. 1597–1612, doi: 10.1002/esp.1112.

Roering, J.J., and Gerber, M., 2005, Fire and the evolution of steep, soil-mantled landscapes: Geology, v. 33, p. 349–352, doi: 10.1130/G21260.1.

Roering, J.J., Kirchner, J.W., and Dietrich, W.E., 1999, Evidence for nonlinear, diffusive sediment transport on hillslopes and implications for landscape morphology: Water Resources Research, v. 35, p. 853–870, doi: 10.1029/1998WR900090.

Roering, J.J., Kirchner, J.W., and Dietrich, W.E., 2001a, Hillslope evolution by nonlinear, slope-dependent transport: Steady-state morphology and equilibrium adjustment timescales: Journal of Geophysical Research, v. 106, p. 16,499–16,513, doi: 10.1029/2001JB000323.

Roering, J.J., Kirchner, J.W., Sklar, L.S., and Dietrich, W.E., 2001b, Hillslope evolution by nonlinear creep and landsliding: An experimental study: Geology, v. 29, p. 143–146, doi: 10.1130/0091-7613(2001)029<0143:HEBNCA>2.0.CO;2.

Roering, J.J., Almond, P., Tonkin, P., and McKean, J., 2004, Constraining climatic controls on hillslope dynamics using a coupled model for the transport of soil and tracers: Application to loess-mantled hillslopes, Charwell River, South Island, New Zealand: Journal of Geophysical Research-Earth Surface, v. 109, p. doi:10.1029/2003JF000034.

Roering, J.J., Kirchner, J.W., and Dietrich, W.E., 2005, Characterizing structural and lithologic controls on deep-seated landsliding: Implications for topographic relief and landscape evolution in the Oregon Coast Range, USA: Geological Society of America Bulletin, v. 117, p. 654–668, doi: 10.1130/B25567.1.

Schmidt, K.M., Roering, J.J., Stock, J.D., Dietrich, W.E., Montgomery, D.R., and Schaub, T., 2001, The variability of root cohesion as an influence on shallow landslide susceptibility in the Oregon Coast Range: Canadian Geotechnical Journal, v. 38, p. 995–1024, doi: 10.1139/cgj-38-5-995.

Smith, T.R., and Bretherton, F.P., 1972, Stability and the conservation of mass in drainage basin evolution: Water Resources Research, v. 8, p. 1506–1529.

Stock, J., and Dietrich, W., 2006, Erosion of steepland valleys by debris flows: Geological Society of America Bulletin, v. 118, p. 1125–1148, doi: 10.1130/B25902.1.

Stock, J., and Dietrich, W.E., 2003, Valley incision by debris flows: Evidence of a topographic signature: Water Resources Research, v. 39, no. 4, 25 p.

Strahler, A.N., 1950, Equilibrium theory of erosional slopes approached by frequency distribution analysis: American Journal of Science, v. 248, p. 673–696.

Torres, R., Dietrich, W.E., Montgomery, D.R., Anderson, S.P., and Loague, K., 1998, Unsaturated zone processes and the hydrologic response of a steep, unchanneled catchment: Water Resources Research, v. 34, p. 1865–1879, doi: 10.1029/98WR01140.

Tucker, G.E., and Slingerland, R.L., 1994, Erosional dynamics, flexural isostasy, and long-lived escarpments: A numerical modeling study: Journal of Geophysical Research, v. 99, p. 12,229–12,243, doi: 10.1029/94JB00320.

van der Beek, P., and Braun, J., 1998, Numerical modelling of landscape evolution on geological time-scales: A parameter analysis and comparison with the south-eastern highlands of Australia: Basin Research, v. 10, p. 49–68, doi: 10.1046/j.1365-2117.1998.00056.x.

Whipple, K., Heimsath, A., Ouimet, W., Crosby, B., and Wobus, C., 2005, The relation between topography and millennial erosion rates in the San Gabriel Mountains, California: Eos (Transactions, American Geophysical Union), v. 86, abstract H51C-0376.

Willett, S.D., 1999, Orogeny and orography: The effects of erosion on the structure of mountain belts: Journal of Geophysical Research, v. 104, p. 28,957–28,981, doi: 10.1029/1999JB900248.

Willgoose, G., Bras, R.L., and Rodriguez-Iturbe, I., 1991, A coupled channel network growth and hillslope evolution model; 1: Theory: Water Resources Research, v. 27, p. 1671–1684, doi: 10.1029/91WR00935.

Yoo, K., Amundson, R., Heimsath, A.M., and Dietrich, W.E., 2005, Process-based model linking pocket gopher (Thomomys bottae) activity to sediment transport and soil thickness: Geology, v. 33, p. 917–920, doi: 10.1130/G21831.1.

Young, A., 1961, Characteristic and limiting slopes: Zeitschrift fur Geomorphologie, v. 5, p. 126–131.

Manuscript received 30 June 2007
Revised manuscript received 28 December 2007
Manuscript accepted 3 January 2008

Printed in the USA